# NASA Analysis of Space Mission Options for the 2025 Planetary Defense Conference Hypothetical Asteroid Impact Threat Scenario

**Brent W. Barbee[1], Justin Atchison[2], Rylie Bull[2], Mary Burkey[3], Wendy K. Caldwell[4], Paul Chodas[5], Jessie Dotson[6], Davide Farnocchia[5], Kelly Fast[7], Lindley Johnson[7], Kathryn M. Kumamoto[3], Josh Lyzhoft[1], Daniel D. Mazanek[8], Ryan S. Park[5], Jason M. Pearl[3], Catherine S. Plesko[4], Isaiah Santistevan[3], Matthew A. Vavrina[9], Lorien Wheeler[6]**

[1]*NASA/Goddard Space Flight Center, Code 595, 8800 Greenbelt Road, Greenbelt, MD, 20771, USA*
[2]*Johns Hopkins University Applied Physics Laboratory, 11100 Johns Hopkins Road, Laurel, MD, 20723, USA*
[3]*Lawrence Livermore National Laboratory, 7000 East Avenue, Livermore, CA, 94550, USA*
[4]*Los Alamos National Laboratory, P.O. Box 1663, Los Alamos, NM 87545, USA*
[5]*Jet Propulsion Laboratory, California Institute of Technology, 4800 Oak Grove Drive, Pasadena, CA, 91109, USA*
[6]*NASA Ames Research Center, MS 245-6, Moffett Field, CA, 94035, USA*
[7]*NASA Headquarters, 300 E St SW, Washington, DC, 20546, USA*
[8]*NASA Langley Research Center, Mail Stop 462, 5 Langley Blvd., Hampton, VA 23681-2199, USA*
[9]*a.i. solutions, Inc., 4500 Forbes Boulevard, Suite 300, Lanham, MD, 20706, USA*

## Abstract

The 2025 Planetary Defense Conference (PDC) hypothetical asteroid impact threat exercise is being conducted in coordination with the United Nations-endorsed Space Mission Planning Advisory Group (SMPAG), exercising SMPAG's processes for assessing space mission options and communicating to decision makers. In this paper, we describe the work performed by our NASA-led team and present the results we contributed to the SMPAG effort for the exercise. Our NASA-led team assessed mission options for asteroid reconnaissance (flyby and rendezvous), deflection, and robust disruption using several viable techniques: kinetic impactors, ion beam deflection, and nuclear explosive devices. Our simulations and analyses considered how much change-in-velocity an asteroid can tolerate before fragmentation onset, and we worked towards establishing requirements for robustly disrupting an asteroid. Heuristics informed by the simulation results are incorporated into optimization of deflection and disruption mission campaign options. Finally, we make some observations about useful generalizations from these results with potential applicability to any planetary defense scenario.

*Keywords: Planetary Defense, Asteroid Deflection, Space Mission Analysis, Spacecraft Trajectory Design*

## 1. Introduction

The 2025 Planetary Defense Conference (PDC) hypothetical asteroid impact threat exercise[1] is being conducted in coordination with the United Nations-endorsed Space Mission Planning Advisory Group (SMPAG)[2], enabling an exercise of SMPAG's process for producing technical recommendations for space mission options using inputs received from space agencies in participating nations. In this paper, we describe the work performed for this exercise by the NASA-led team. We also note that there was good agreement between the analysis results generated by our team and the other participating teams.

We discuss our methodologies for assessing space mission and campaign options for responding to the hypothetical scenario using a variety of approaches, including reconnaissance, deflection, and disruption. For reconnaissance, we assess flyby and rendezvous options and we include both re-tasked extant spacecraft and purpose-built spacecraft. Detailed results for analysis of re-tasking extant spacecraft for reconnaissance are also presented in a related paper [1]. For Earth impact prevention missions, both asteroid deflection and robust disruption of the asteroid are considered, and the following mission types are assessed: Kinetic Impactor (KI) deflection and disruption, Ion Beam Deflection (IBD), and Nuclear Explosive Device (NED) deflection and disruption.

We also summarize simulation studies performed to 1) ascertain how much change-in-velocity (ΔV) an asteroid can tolerate before fragmentation onset; and 2) establish requirements for robustly disrupting an asteroid, i.e., breaking it into small and widely scattered fragments posing little to no residual Earth impact risk. Heuristics informed by simulation results are incorporated into optimization of multi-action deflection mission campaign options that spread the total deflection impulse across multiple smaller impulses as a strategy for avoiding asteroid fragmentation during deflection. Studies were also performed assessing the minimum amount of time required between deflection impulses to measure their effect on the asteroid's orbit before the next impulse. Details of that study are presented in a related paper [2].

We assess mission options at two epochs in the scenario timeline: Epoch 1, about two months post-discovery when Earth impact probability climbs above the 1% threshold for SMPAG involvement and large uncertainties in asteroid physical properties and Earth impact location drive large uncertainties in mission requirements; and Epoch 2, just after a flyby reconnaissance mission has reconnoitered the asteroid, significantly reducing uncertainties in asteroid physical properties and Earth impact location and thus enabling more precise assessments of mission options.

Finally, we summarize the results we provided as inputs from NASA to SMPAG for integration with all such results from other space agencies participating in this

[1] For hypothetical asteroid impact threat exercise scenario details, please visit https://cneos.jpl.nasa.gov/pd/cs/pdc25/ (last accessed 2025-07-27).
[2] For more information about SMPAG, please visit https://smpag.net/ (last accessed 2025-10-17).

exercise. We also make some observations about useful generalizations from these results with potential applicability to any planetary defense scenario.

## 2. Hypothetical Asteroid Impact Threat Scenario Overview

As part of the activities for the 2025 Planetary Defense Conference, a realistic impact scenario was designed. The main goal of the scenario was that of exercising the readiness to respond to an asteroid impact threat, including the involvement of SMPAG.

The selected hypothetical asteroid is on an impact trajectory for 2041 April 24. The absolute magnitude of the asteroid is H = 21.9, which roughly corresponds to a diameter in the range of 100-250 meters for an albedo between 5% and 25%. Fig. 2.1 shows the orbit of the asteroid, which has a semimajor axis of 1.7 au (and therefore an orbital period of 2.1 years), an eccentricity of 40%, and an inclination of 11 deg.

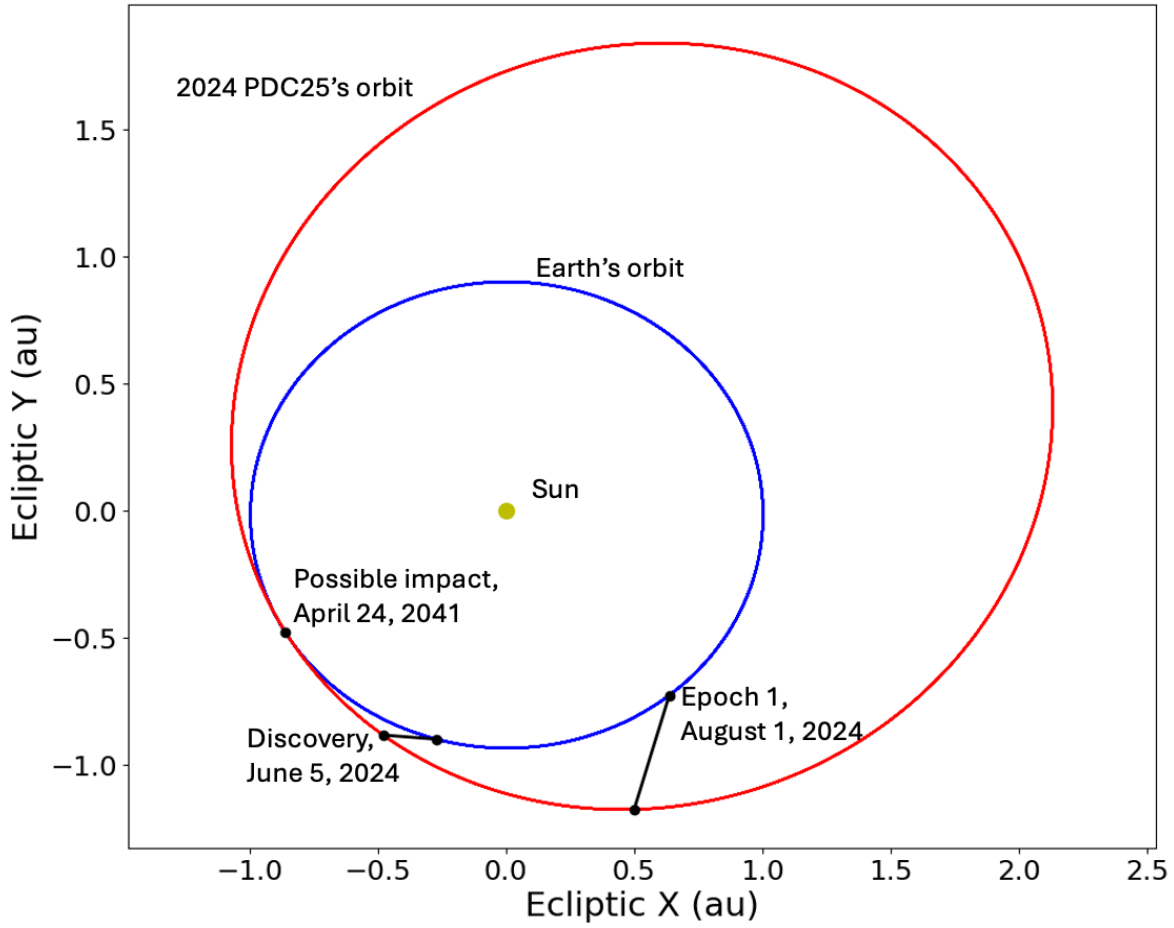



**Fig. 2.1: Orbit of hypothetical asteroid 2024 PDC25 (red) relative to the Earth (blue) projected onto the ecliptic plane. The discovery, epoch 1, and impact configurations are marked.**

The hypothetical asteroid was "discovered" by the Catalina Sky Survey [3] on 2024 June 6, when it was at a solar elongation of 90 deg and became bright enough (apparent magnitude of V = 21.5) to be observed from the ground. The asteroid's

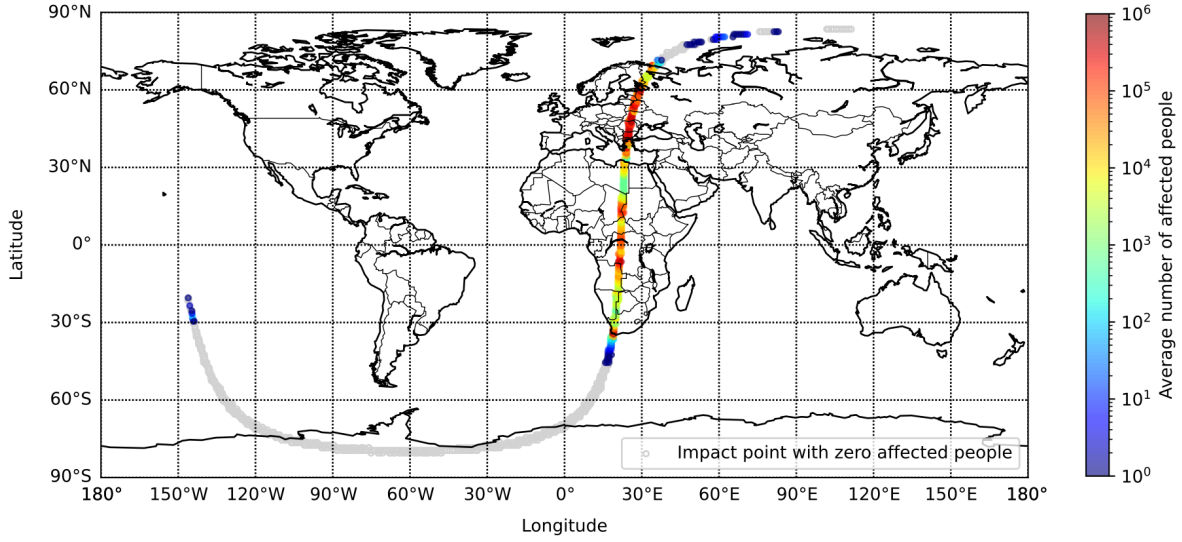
designation is 2024 PDC25, which is not a permissible designation for a real asteroid because three letters are not allowed.

*2.1 Epoch 1*

After discovery, we simulated a realistic cadence of observations to assess the amount of information that would be available over time. The impact in 2041 is immediately recognized as a possibility, but with a very small initial probability, about 1 in 10,000. Epoch 1 of the exercise is set to 2024 August 1, when, after nearly two months of tracking, the probability of impact reaches 1.6%. This impact probability is larger than the 1% threshold and therefore triggers a notification to SMPAG by the International Asteroid Warning Network (IAWN)[3].

The physical properties of 2024 PDC25 are mostly constrained by infrared observations from the James Webb Space Telescope [4]. The asteroid's diameter is likely in the range of 90–160 m, with a median diameter size of 125 m and a full range of 50–280 m. Moreover, the asteroid belongs to the S-type taxonomic class [5], which implies a stony composition and favors a bulk density between 1.6 and 2.7 g $cm^{-3}$ [6].

Although an impact is unlikely at this stage, the corridor of possible impact locations can already be constrained. Fig. 2.2 shows the potential impact corridor, which extends from the Russian Laptev, Kara, and Barents Seas, across Eastern Europe, the Mediterranean Sea, and Africa to the Cape of Good Hope, across the South Atlantic and Antarctic coast, and ends in the South Pacific. The impact locations are colored by the average affected population estimates produced by the NASA Probabilistic Asteroid Impact Risk (PAIR) modeling [7A] performed for the exercise, available on the exercise scenario website[1].The affected population estimates depend on the impact location and the mass of the asteroid, along with other entry and damage factors, all of which remain highly uncertain at this time.




[3] https://cneos.jpl.nasa.gov/pd/cs/pdc25/PDC25-IAWN_Impact_Notification1.pdf (last accessed 2025-10-17). For more information about IAWN, please visit https://iawn.net/ (last accessed 2025-10-17).

**Fig. 2.2: Average affected population along potential impact regions for 2024 PDC25 at Epoch 1.**

2024 PDC25 can still be tracked with astrometric observations through mid-December 2024, when it will then become unobservable from Earth until August 2025 through mid-November 2026. These additional observations will reduce prediction uncertainties and refine the probability of an impact in 2041. No additional information on the size of 2024 PDC25 can be obtained without deep-space radar observations, which are not possible until 2041, or without observations from a spacecraft encounter with the asteroid.

*2.2 Epoch 2*

For Epoch 2 of the PDC25 impact scenario, time fast-forwards by four years. Thanks to additional tracking from the ground, the probability of impact in 2041 reached 100% in September 2025. In response to the IAWN notification, SMPAG issued several recommendations, including a fast flyby reconnaissance mission. We therefore simulated a mission that flew by 2024 PDC25 on 2028 April 12 at a relative velocity of 8 km/s. Epoch 2 is set to 2028 April 28, when the results from the flyby mission become available.

The data collected during the flyby confirm that 2024 PDC25 is an S-type asteroid and greatly reduces its size uncertainty, as shown in Table 2.1. The asteroid has a spherical equivalent diameter of 145−155 m, with an elongated shape around twice as long as it is wide. The flyby data also measured the rotation period (3 hours), thermal inertia (200 ± 20 J $m^{-2}$ $K^{-1}$ $s^{-1/2}$), and spin axis (RA = 253 deg, Dec = 74 deg, with an uncertainty of 3 deg). This physical characterization results in a Yarkovsky drift [7] of 586 ± 195 m/yr. Moreover, optical navigation measurements during the approach and flyby greatly refine orbital predictions.

The region of possible impact locations is now reduced to a 470-km corridor across the border between Angola and the Democratic Republic of the Congo (see Fig. 2.3[4]). Combining the derived physical properties with the impact velocity of 13.8 km/s results in impact energies from 45−160 Mt, most likely from 60−105 Mt. The entry parameters for the impact points shown in Fig. 2.3 vary only slightly among the points, and they are well known for given points. The entry velocities span 13.723−13.728 km/s, the entry angles are moderately steep, spanning 67°−71° from horizontal, and the entry flight directions (headings) are all nearly directly northward.

[4] From https://cneos.jpl.nasa.gov/pd/cs/pdc25/epoch2.html.

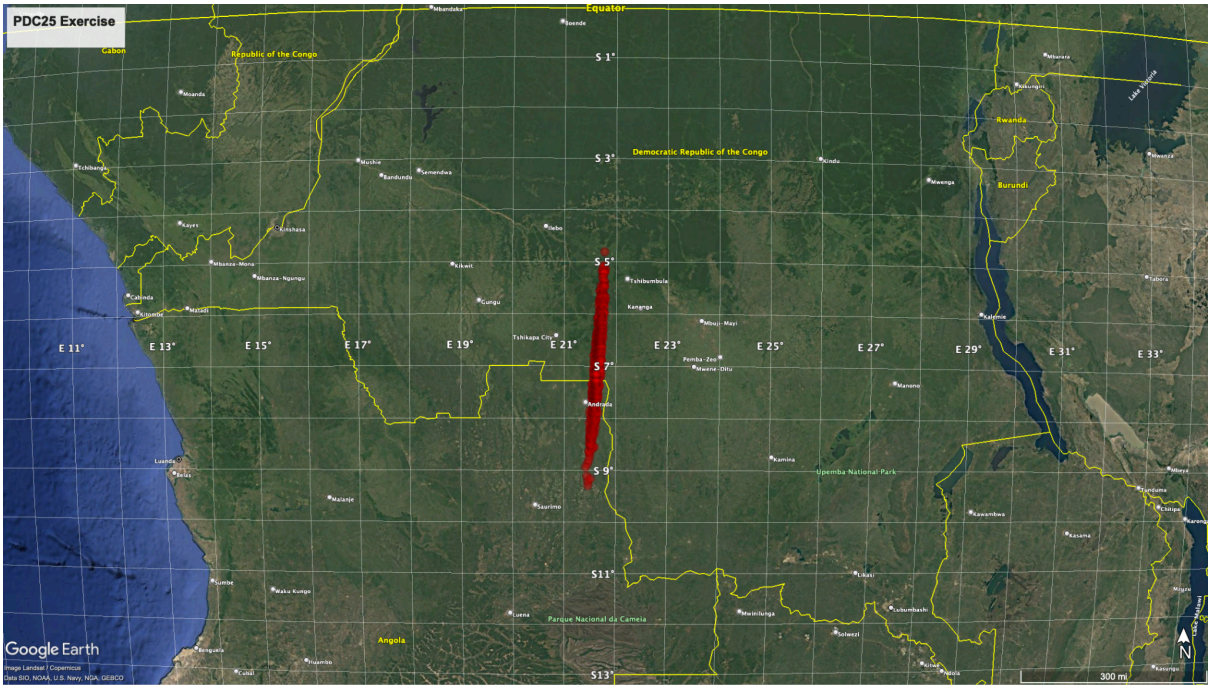



**Figure 2.3: Impact footprint across the border between Angola and the Democratic Republic of the Congo as constrained by the flyby data.**

**Table 2.1. Asteroid Physical Properties at Epoch 2.**

| Physical Property | Lowest Mass | Low Mass | 5th Mass Percentile | 25th Mass Percentile | 50th Mass Percentile | 75th Mass Percentile | 95th Mass Percentile | High Mass | Highest Mass |
|---|---|---|---|---|---|---|---|---|---|
| Diameter (m) | 147 | 152 | 149 | 149 | 150 | 151 | 152 | 154 | 155 |
| Bulk Density (g/cm3) | 1.211 | 1.128 | 1.514 | 1.902 | 2.207 | 2.54 | 2.968 | 3.372 | 3.598 |
| Porosity | 0.595 | 0.596 | 0.57 | 0.402 | 0.313 | 0.244 | 0.093 | 0.062 | 0.039 |
| Mass (billion kg) | 2.00 | 2.09 | 2.60 | 3.31 | 3.93 | 4.59 | 5.49 | 6.41 | 7.03 |
| Surface Escape Velocity (cm/s) | 6.05 | 6.04 | 6.85 | 7.68 | 8.33 | 9.00 | 9.79 | 10.57 | 10.99 |
| Absolute Magnitude | 21.42 | 21.98 | 22.16 | 21.24 | 21.6 | 21.59 | 21.58 | 21.86 | 22.28 |
| Albedo | 0.221 | 0.123 | 0.109 | 0.253 | 0.179 | 0.179 | 0.178 | 0.135 | 0.09 |
| Taxonomic Type | S | S | S | S | S | S | S | S | S |
| Best-fit Ellipsoid Axis 2a (m) | 115 | 122 | 123 | 120 | 119 | 119 | 121 | 112 | 126 |
| Best-fit Ellipsoid Axis 2b (m) | 118 | 122 | 116 | 115 | 117 | 120 | 124 | 125 | 126 |
| Best-fit Ellipsoid Axis 2c (m) | 235 | 237 | 230 | 241 | 244 | 242 | 236 | 259 | 234 |

## 3. Deflection Requirements

The requirements for deflecting the asteroid are framed in terms of 1) the distance that the asteroid's B-plane coordinates [8] must be moved in the B-plane in order to move the asteroid's potential impact locations completely off the Earth; and 2) the change in the asteroid's velocity (ΔV) required to move the asteroid by the necessary distance in the B-plane to achieve deflection off of the Earth.

*3.1 Epoch 1*

During Epoch 1, the uncertainty in the asteroid's Earth impact location spans the entire impact risk chord in the B-plane. Because KIs can only deflect southward, this means that the worst-case deflection distance for KIs is the full chord length, which would occur if the asteroid's Earth impact location happened to be at the northern Earth limb and the KIs then had to deflect the asteroid by the entire chord length in the southward direction. KIs can only deflect southward because that direction corresponds to slowing the asteroid down, which can be achieved by placing the spacecraft on a smaller (and easier to launch into) orbit around the Sun than the asteroid's orbit. In that case, the spacecraft is moving more slowly than the asteroid when impacting the asteroid at the asteroid's perihelion, and therefore slows the asteroid down. Deflecting northward would require speeding the asteroid up, which would require the spacecraft to be launched into an even higher orbit around the Sun than the asteroid's orbit, such that the spacecraft would be traveling faster than the asteroid when impacting it at perihelion. That proves to be impractical, because relatively little spacecraft mass (or no mass at all) can be launched into such a large orbit around the Sun due to current limitations on launch vehicle capabilities. Because IBD and NED can deflect northward or southward, the worst-case deflection distance for IBD and NED is half of the chord length, corresponding to the asteroid's Earth impact location in the B-plane being at the geocenter. To illustrate how the deflection ΔV requirement may vary depending on what the asteroid's Earth impact location actually turns out to be, Figure 2.4 shows the along-track ΔV required for deflection as a function of the time at which the ΔV is applied to the asteroid, for the full chord, half chord, quarter chord, and one-tenth chord. The along-track direction for ΔV maximizes the deflection distance represents the minimum ΔV required to achieve a given deflection distance in the B-plane.

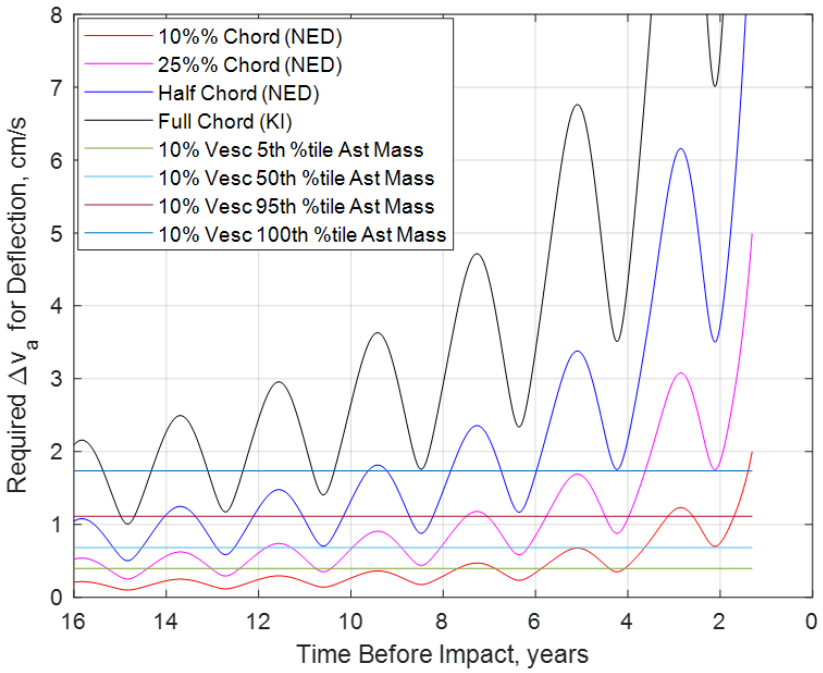



**Figure 2.4: Required along-track ΔV for deflecting the asteroid by various fractions of the impact risk chord length. Horizontal lines corresponding to 10% of the escape velocity for the 5th, 50th, 95th, and 100th percentile asteroid masses are shown for reference. ΔV above 10% escape velocity could risk unwanted asteroid fragmentation.**

*3.2 Epoch 2*

The flyby reconnaissance mission significantly reduces uncertainties in both the asteroid's physical properties and Earth impact location. Figure 2.5 shows the post-reconnaissance Earth impact uncertainty region and the corresponding northward and southward deflection distances in the B-plane required to move the asteroid off the Earth.

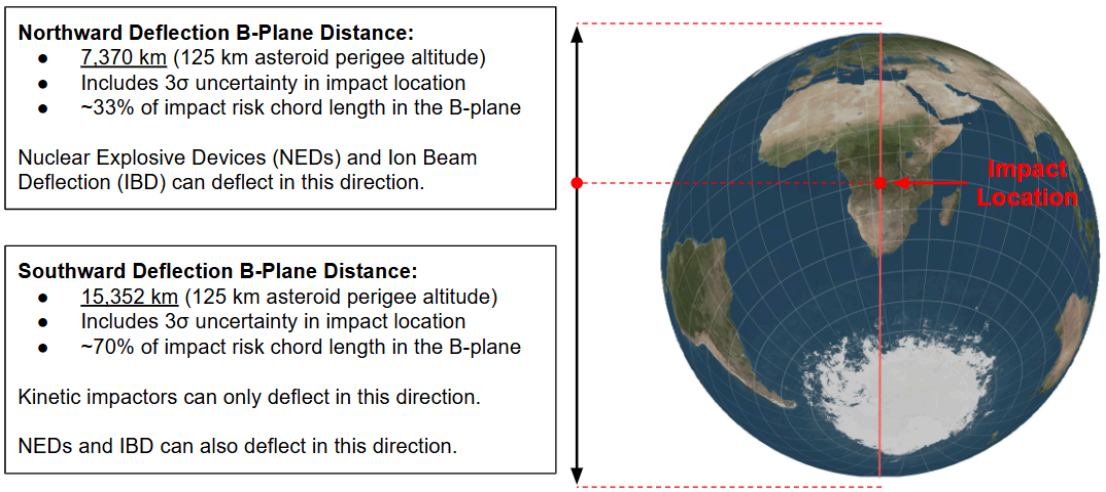



**Figure 2.5: Northward and southward B-plane deflection distance requirements at Epoch 2.**

Since the asteroid's size is now known with a much higher degree of certainty, and since its smaller size would not result in a significantly affected impact area, the option of a partial deflection to an ocean location sufficiently far from land is a possible mitigation option to be considered. Figure 2.6 shows a notional safe zone for a partial deflection in which the asteroid would be moved southward and allowed to impact over the ocean around 50.2 deg south latitude. Preliminary simulation of airwave-driven (Lamb wave) tsunami from a 160-megaton airbust (the upper end of the Epoch 2 energy range) suggests that this ocean impact location would not place populations along the southern coast of Africa or the Antarctic ice shelf at risk of adverse effects. This simulation was performed using GeoClaw [9A] with shallow-water equations driven by airwave pressure forcing. However, the analysis is preliminary and further assessment of newly studied airwave-driven global tsunami hazards [9B] would be needed to be certain as to whether the partial deflection would truly be considered safe and acceptable.

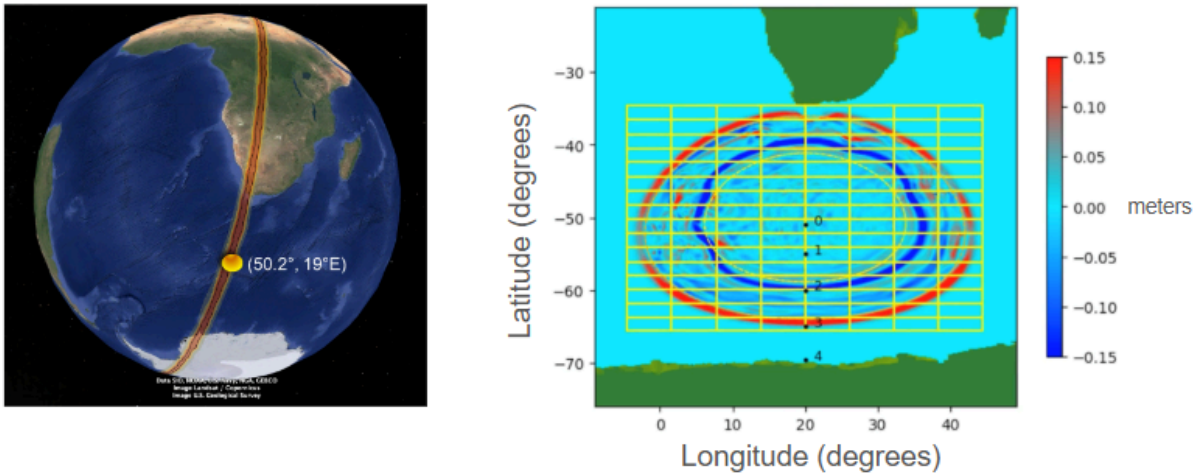



**Figure 2.6. Preliminary target zone for southward partial deflection (left) and exemplar preliminary airwave-driven (Lamb wave) tsunami simulation output (right).**

Although not readily apparent from the map projection used in Figure 2.5, the southward deflection distance is approximately twice the northward deflection distance. The associated along-track ΔV required for northward, southward, and partial southward deflection are shown in Figure 2.7, along with horizontal reference lines for 10% escape velocity for the Low, 50th Percentile, and High asteroid masses from Table 2.1.

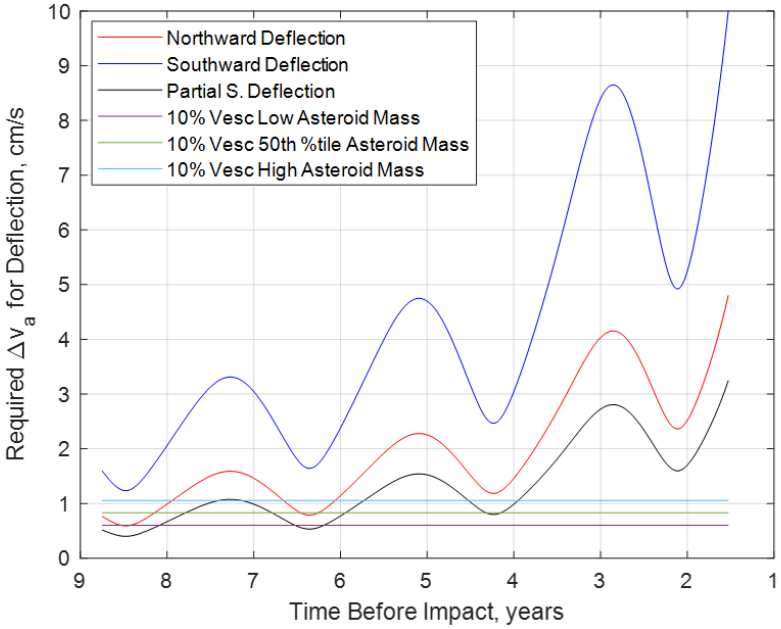



**Figure 2.7: Required along-track ΔV for deflecting the asteroid by the northward, southward, or partial southward deflection distances. Horizontal lines corresponding to 10% of the escape velocity for the Low, 50th Percentile, and High asteroid masses are shown for reference. ΔV above 10% escape velocity could risk unwanted asteroid fragmentation.**

*3.3 Deflection vs. Disruption*

The question of how much ΔV an asteroid can tolerate during deflection and remain intact, i.e., be deflected without unwanted fragmentation, remains an area of active research. The question of how much ΔV must be imparted to an asteroid in order to robustly disrupt it also remains an area of active research. Robust disruption is the deliberate, forceful disruption of an asteroid via an applied impulse such that the largest remaining fragment is no larger than about 10 m and the fragments are all widely dispersed. Ten meters is the fragment size that should be shielded against Earth impact by our planet's atmosphere. Wide dispersal of the fragments results in none, or at most a tiny fraction, of the asteroid's original mass going on to interact with the Earth-Moon system in the future. The efficacy of using imparted ΔV as the best proxy for assessing fragmentation/disruption also remains under investigation, along with various alternative approaches, including energy-based metrics.

In lieu of in situ investigations, detailed and time-consuming hydrocode simulations are crucial for exploring the onset of fragmentation, or the conditions for robust disruption of asteroids. Model predictions are sensitive to physical properties such as the porosity, density, strength, asteroid rotation, and more, and there is no full-scale disruption mission that has been demonstrated to validate these models. As such, uncertainty quantification is important for assessments like these. Ideally, to address this uncertainty, ensemble simulations, including resolution and sensitivity studies, should be performed over a range of model parameters and property uncertainties to report probabilities of varying levels of success for mission-relevant outcomes, such as robust disruption or accidental fragmentation. Establishing such acceptable risk thresholds for these probabilities is a policy decision, and is beyond the scope of this

work.. However, computational limitations prevent such ensemble simulations from being run to longer than several seconds of simulation time, far shorter than what is required to understand the outcomes. While work continues to improve the capability to run longer simulation times for affordable amounts of “wall-clock time,” heuristics for the onset of fragmentation and for the requirement for robust disruption have been developed by examining the rapid expansion of asteroid bodies in impact simulations.

These studies [9,10] have yielded a heuristic for avoiding unwanted fragmentation of $\Delta V \leq 10\%\ V_{escape}$, and a heuristic for robust disruption of $\Delta V \geq 1{,}000\%\ V_{escape}$, where $V_{escape}$ is the asteroid’s surface escape velocity. We adopt these heuristics for our mission analysis herein, while acknowledging that ongoing work may yield improved heuristics in the future.

The KI trajectory imparting maximum ΔV to the asteroid was identified within the trajectory solution space, launching on 2032-04-07 with an Earth departure characteristic energy ($C_3$) of 4.951 $km^2/s^2$ and having a mass of 13,633 kg (launching on a Falcon Heavy Expendable launch vehicle). It strikes the asteroid at 10.24 km/s. The ΔV imparted to the Low-, 50th Percentile-, and High-mass realizations of the asteroid would be 229%, 86%, and 36% of $V_{escape}$, respectively. All of those are clearly much less than 1000% $V_{escape}$ threshold for robust disruption. From these results, we ruled out kinetic robust disruption as a viable means of Earth impact prevention in this scenario.

We also assessed the maximum ΔV that could be imparted to each realization of the asteroid via a NED with one megaton (Mt) of explosive energy using approximate empirical models [11,12,13]. The ΔV that could be imparted ranged from 226% to 800% $V_{escape}$, with a median of 400% $V_{escape}$—again, all less than the 1,000% $V_{escape}$ threshold for robust disruption. From these results, we determined that robust disruption of the asteroid in this scenario via NED would not be viable without going to significantly higher energy levels.

The methods employed for these analyses are approximate and assume only a single KI or NED is being used to effect robust disruption, and so further work is required to produce more refined results. For purposes of the mission analysis in this scenario we elected to set aside robust disruption of the asteroid and instead concentrate on deflection as the means of Earth impact prevention. We also adopt the heuristic of $\Delta V \leq 10\%\ V_{escape}$ and enforce it in our mission designs in order to avoid unwanted fragmentation of the asteroid during deflection. The question of whether some amount of asteroid fragmentation during deflection would actually be acceptable is relegated to future work.

We note that the smaller, lower mass realizations of the asteroid in the Epoch 1 data resulted in many cases of robust disruption by a single kinetic impactor, as well as many cases of likely disruption. The constrained asteroid mass, density, and axis measurements used in Epoch 2 further demonstrate the benefit of a flyby reconnaissance mission to reduce uncertainties in the parameter space and increase fidelity in computational results.

## 4. Reconnaissance Mission Analysis

Options for sending a spacecraft to reconnoiter the asteroid were considered, including the re-tasking of extant spacecraft or conducting dedicated flyby and rendezvous missions.

### *4.1 Re-Tasking of Extant Spacecraft*

It is possible to redirect an already inflight spacecraft to survey the asteroid in addition to, or instead of, a dedicated mission. Doing so can potentially reach the asteroid before a purpose-built mission could because the development and launch has already been accomplished. Of the currently operating NASA small body missions, we find that either the Lucy spacecraft or the Origins, Spectral Interpretation, Resource Identification and Security – Apophis Explorer (OSIRIS-APEX) could be re-tasked to perform fast flybys of 2024 PDC25 by retargeting their respective Earth gravity assists [1]. Lucy could arrive at the asteroid as soon as June 2026, nearly two years before a purpose built flyby mission could arrive. However, the decision to divert would need to be made before Lucy's December 2024 Earth gravity assist (EGA), before the impact probability would reach 100%. Lucy would not be able to return to its original mission, making this option unattractive.

OSIRIS-APEX could reach the asteroid in July 2028, comparable with a dedicated mission, by retargeting its March 2027 EGA. Figure 4.1 shows the redirect trajectory, where the divert maneuver is done in January 2026, after the Earth impact probability would have risen to 100%. While potentially appealing, OSIRIS-APEX was designed for asteroid rendezvous, not a fast flyby, and re-tasking it would require additional analysis for the suitability of the spacecraft's payload suite and guidance, navigation, and control systems. Figure 4.2 shows the expected performance of the PolyCam imager, OSIRIS-APEX's narrow angle camera, that would be used for initial asteroid detection and navigation on approach. Initial detection could be made only a handful of days before the flyby for the 50th Percentile asteroid during Epoch 1. This would make for a challenging operational timeline, but could be feasible if a dedicated mission could not be implemented.

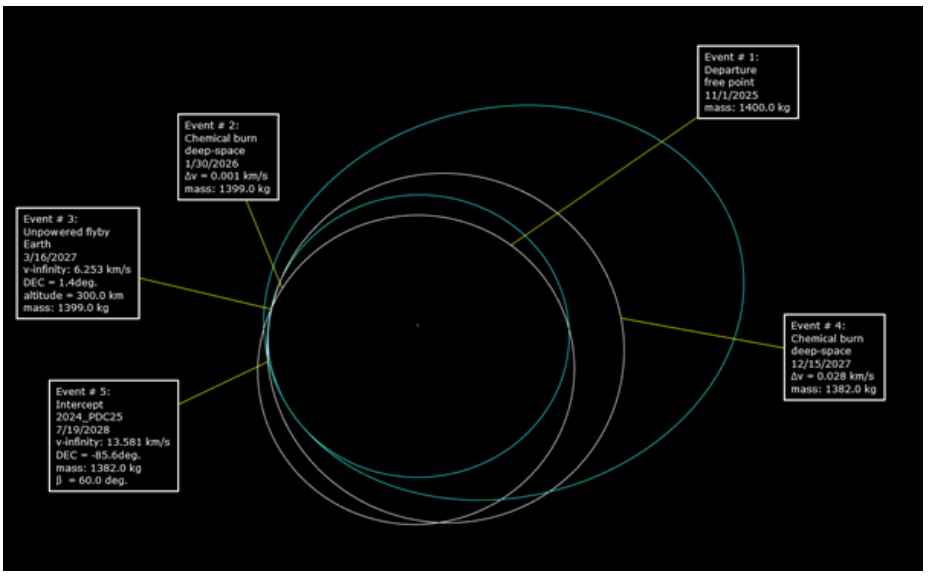



**Figure 4.1: Candidate trajectory to redirect OSIRIS-APEX to a fast flyby of 2024 PDC25. Figure adapted from Bull et al. [1].**

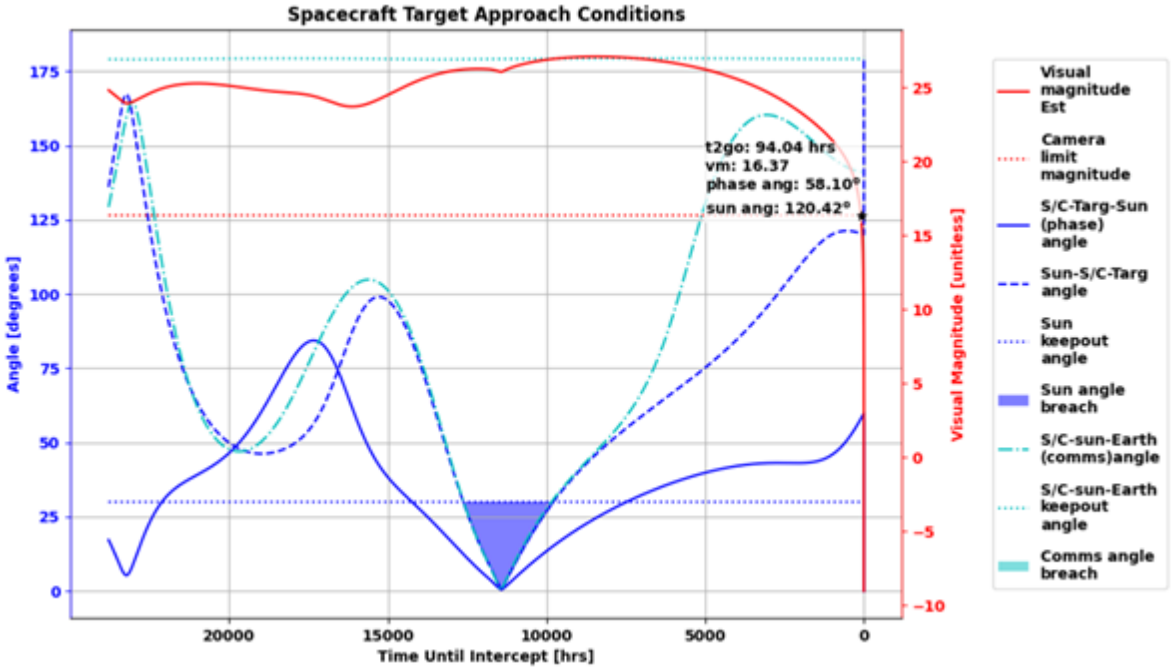



**Figure 4.2: Expected performance of OSIRIS-APEX's PolyCam for the 50th Percentile asteroid for the PDC 2025 exercise. Minimum signal-to-noise: 7; Exposure time: 500 milliseconds; Stacked images: 100. Figure adapted from Bull et al. [1].**

*4.2 Flyby Reconnaissance Missions*

As an alternative to retasking an existing in-space asset, a dedicated flyby reconnaissance mission can be tailored for 2024 PDC25 and potentially allow for improved measurements of the asteroid's physical characteristics. A key consideration for a dedicated flyby mission is the spacecraft development time given the criticality of arriving as early as possible for incorporation of asteroid property measurements into the mitigation campaign. Assuming a minimum of three years is

needed to develop and launch the spacecraft, the earliest allowed launch date is late September 2027, roughly three years after an Authority to Proceed (ATP) is given in October 2024 when the impact probability reaches 10%.

A broad search for high-performing flyby trajectories is conducted by applying a many-objective, stochastic optimization strategy with the objective functions listed in Table 4.1. The trajectory parameters varied within the optimization framework are also listed in Table 4.1. Gravity assists from Venus, Earth, and Mars are considered and deep-space maneuvers (DSMs) are traded with the goal of improving performance of the objective functions. A representation of the globally-optimal Pareto front for delivered mass, arrival date, and flyby speed is depicted in Figure 4.3. The top-performing solutions in terms of delivered mass arrive near the asteroid's ascending node at one AU in October 2030. Arriving near the ascending node minimizes the required orbital plane change to reach the asteroid. Notably, a family of solutions with arrival in early 2028 is apparent in the lower left section of the plot. This family of solutions provides the earliest possible arrival given the assumed launch date constraint, delivering ~500 kg during the flyby.

**Table 4.1: Flyby Reconnaissance Trajectory Optimization Variables (left) and Objective Functions (right)**

| **Trade Parameters** | **Values** |
|---|---|
| **Launch vehicle** | Falcon Heavy Recovery, Vulcan VC4, Falcon Heavy Expendable |
| **Launch date** | October 2027 (ATP+3 years) to October 2032 |
| **Time of flight** | Up to 3 years (arrive no later than October 2036) |
| **Arrival $V_\infty$** | 1 to 12 km/s |
| **Deep space maneuver magnitude constraint** | <2 km/s |

| **Objectives** |
|---|
| Maximize delivered mass |
| Minimize time of flight |
| Minimize launch date |
| Minimize launch vehicle class |
| Minimize arrival $V_\infty$ |

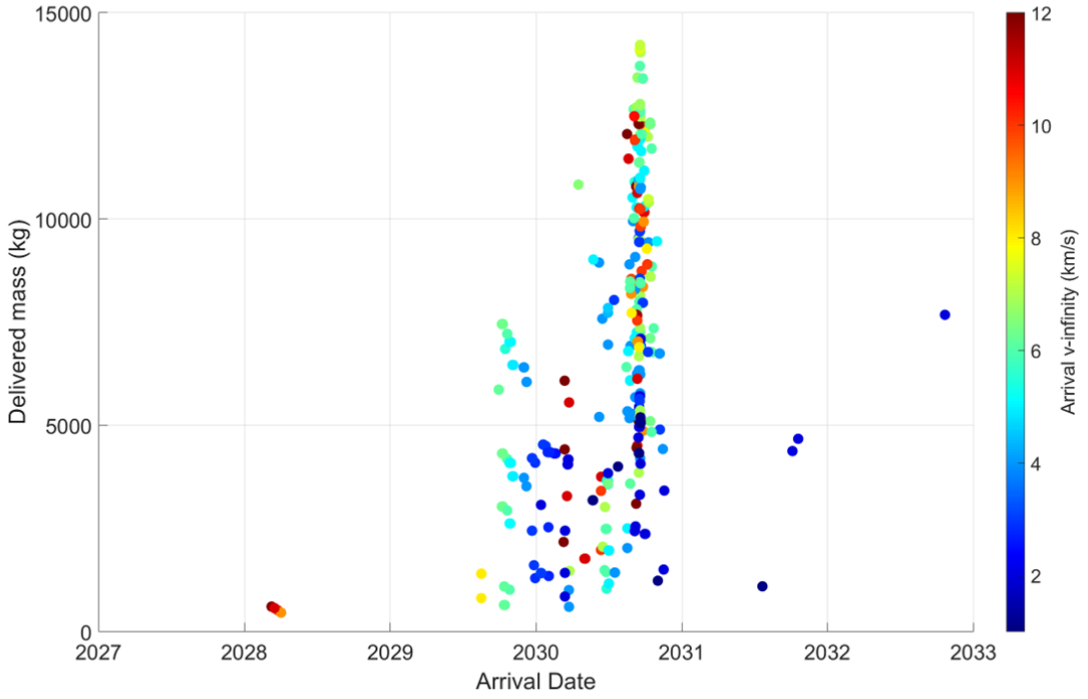



**Figure 4.3: Pareto-optimal solutions for flyby reconnaissance missions with launch no earlier than September 2027.**

The selected flyby reconnaissance trajectory for Epoch 2 launches on September 29, 2027 and arrives at the asteroid on April 12, 2028 with a flyby speed of 8 km/s, as shown in Figure 4.4. The flyby spacecraft launches on a Falcon Heavy Expendable launch vehicle (LV) with a $C_3$ of 95.7 $km^2/s^2$ and executes a 2 km/s DSM one month after launch. The high-$C_3$ launch limits the initial wet mass to 1,029 kg, and the delivered mass after the DSM is 542 kg, which is similar to the dry mass of NASA's Double Asteroid Redirection Test (DART) spacecraft. The spacecraft trajectory relative to the asteroid near close approach is depicted in Figure 4.5. The spacecraft approaches the asteroid at a solar phase angle of approximately 25 degrees, and has a close approach distance of 100 km.

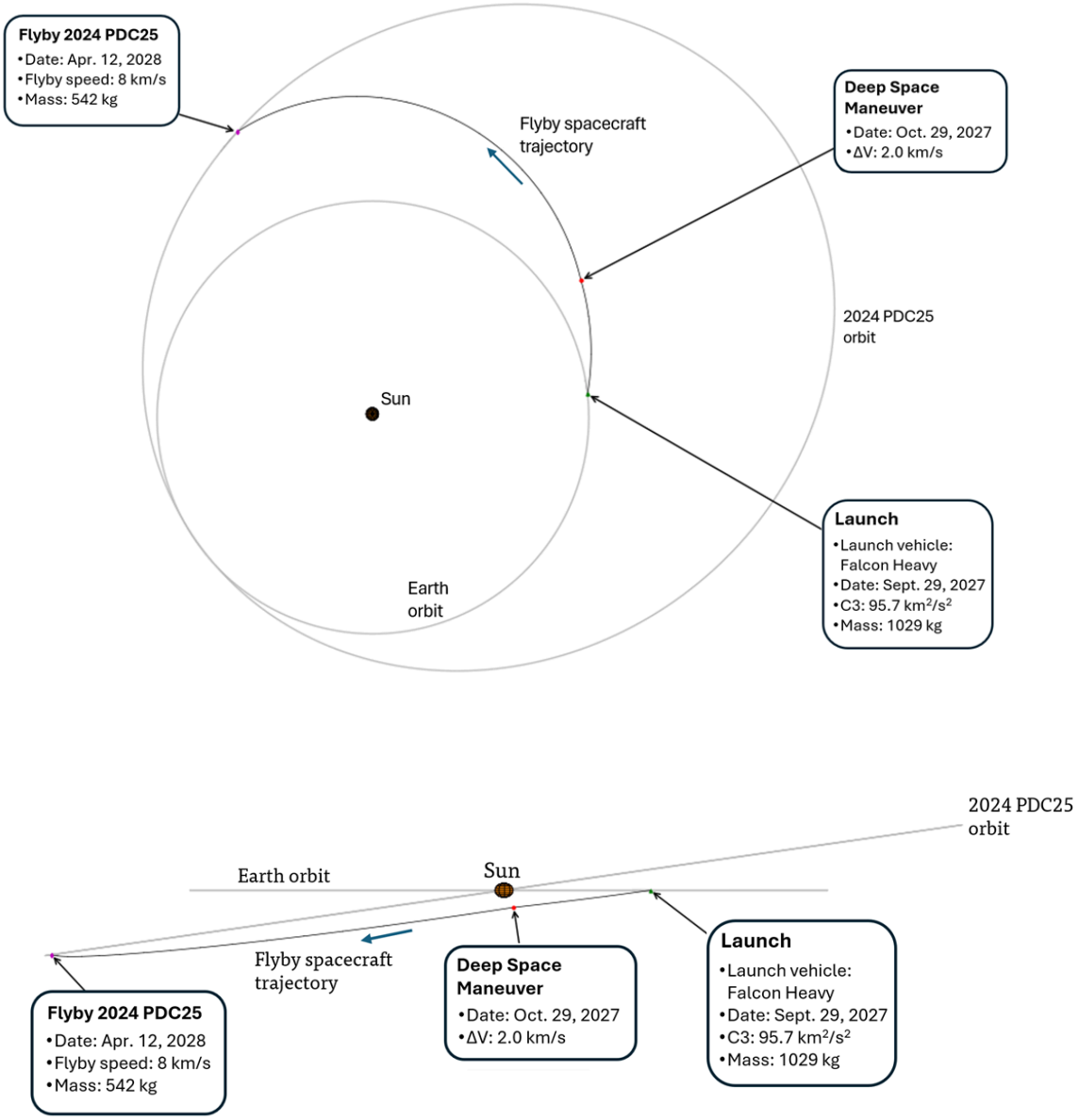



**Figure 4.4: Fast flyby reconnaissance spacecraft trajectory from Earth to 2024 PDC25, as seen in an ecliptic plane view (top) and as seen looking at the ecliptic plane edge-on (bottom).**

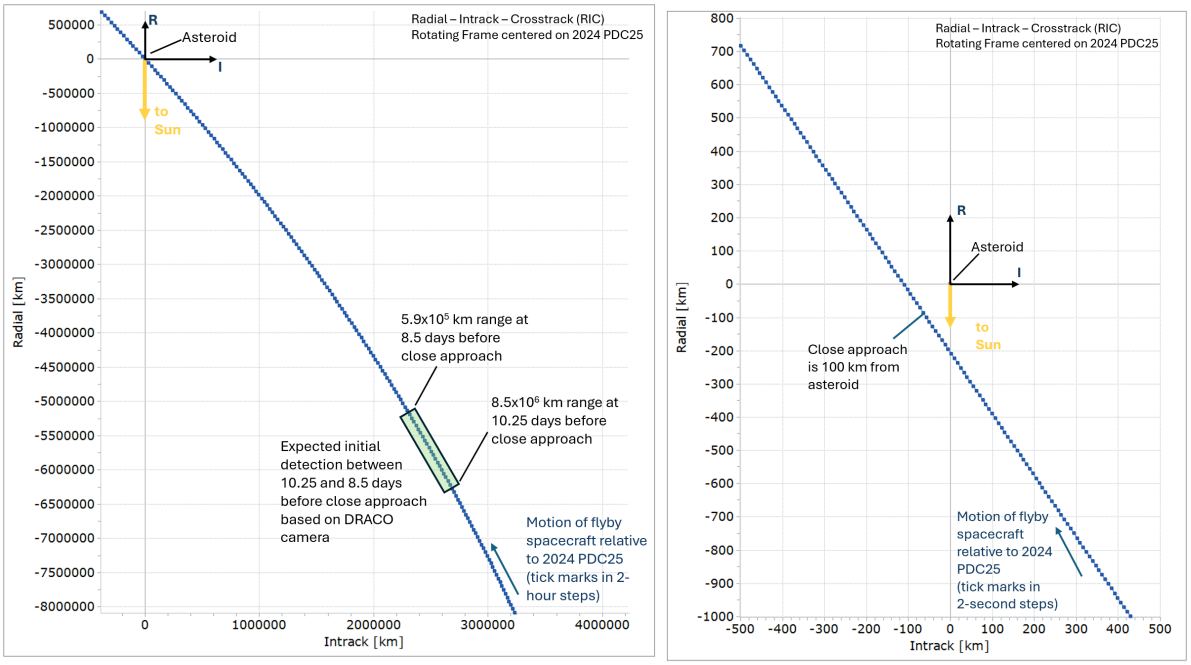



**Figure 4.5: Plots of the flyby spacecraft relative to the asteroid in the asteroid-centered radial-intrack-crosstrack frame. The far-field plot (left) starts ~12 days from close approach and indicates the approximate range when initial detection of the asteroid would be possible with a camera based on the DRACO camera. The near-field plot (right) is a zoom-in and shows the flyby geometry in the radial-intrack plane around the close approach.**

The overall objective of the flyby reconnaissance mission is to provide sufficient actionable information about the asteroid as quickly as possible. Specifically, the flyby spacecraft is meant to refine the impact location, determine the asteroid's size, determine if the asteroid is mostly rocky or mostly metallic, determine if there are multiple objects, and determine the asteroid's surface characteristics (*e.g.*, monolithic vs. rubble pile) [14]. Because payloads can drive a mission's development schedule by increasing the number of interfaces and associated integration and test activities, we advocate for a minimum set of high-heritage instruments to achieve these measurements: a narrow angle camera, a wide angle camera, and a thermal infrared spectrometer. Each of these payload types has multiple U.S. and international flight heritage options that would be sufficient for this flyby encounter. We assess that this instrument suite would return a best-fit triaxial ellipsoid of the asteroid to ±5 meters, reduce the total volume uncertainty to <5% 1σ, and detect a secondary asteroid as small as 10 meters in diameter.

### *4.3 Rendezvous Reconnaissance Missions*

Rendezvous reconnaissance enables accurate measurement of the asteroid's mass and provides an in situ observing spacecraft during mitigation operations. Rendezvous trajectory options to 2024 PDC25 are characterized by high ΔV given the ~10 degree inclination and the relatively high eccentricity of the asteroid's orbit. As such, solar electric propulsion (SEP) provides the necessary propellant efficiency to deliver the payload mass needed for a rendezvous mission. As with the flyby reconnaissance trajectory search, a many-objective optimization routine was utilized to trade key trajectory parameters (launch date, time of flight, SEP thrust profile,

etc.), as well spacecraft propulsion systems parameters such as the launch vehicle, solar array power, and number of thrusters, as listed in Table 4.2.

**Table 4.2: Rendezvous Reconnaissance Trajectory Optimization Variables (left) and Objective Functions (right).**

| Trade Parameters | Values |
|---|---|
| **Launch vehicle** | Falcon 9 RTLS, Falcon 9 ASDS, Falcon Heavy Recovery, Vulcan VC4, Falcon Heavy Expendable |
| **Launch date** | October 2027 (ATP+3 years) to October 2032 |
| **Time of flight** | Up to 4 years |
| **End of life power** | 6 to 34 kW |
| **Number of thrusters** | 1 to 5 |

| Objectives |
|---|
| Maximize delivered mass |
| Minimize time of flight |
| Minimize launch date |
| Minimize launch vehicle class |
| Minimize end of life power |
| Minimize number of thrusters |

The delivered mass versus arrival date of Pareto-optimal solutions from the rendezvous trajectory search are illustrated in Figure 4.6. The color of each solution in the plot indicates the end-of-life (EOL) solar array power available for the SEP system, ranging from 6 kW (blue) to 34 kW (red). The trend of higher power levels enabling higher delivered mass within a launch class is apparent with solutions associated with 26 to 34 kW SEP systems capable of delivering over 10,000 kg to the asteroid for longer flight times. Sub-optimal arrival date gaps in 2032 and 2034 are also apparent in the plot due to the asteroids phasing with Earth. Large mass delivery and short flight times are possible for SEP systems with power levels at or below the Psyche spacecraft 21-kW power level as illustrated in the list of example options in Table 4.3. Moreover, 8- to 12-kW SEP systems similar to the Dawn spacecraft's 10-kW power level can deliver high delivered mass for flight times around two years. A range of launch dates and arrival dates are possible with the earlier launch dates providing the advantage of earlier arrival dates at the cost of a shortened spacecraft development timeline. With the assumption that at least five years from ATP is needed for developing and building a SEP rendezvous reconnaissance spacecraft (RRS), trajectory Case 11 with a launch in December 2029 and arrival in December 2031 affords delivery of 1,911 kg with a 16-kW SEP system. This SEP system and mass are in family with the SEP spacecraft developed for the Psyche mission.

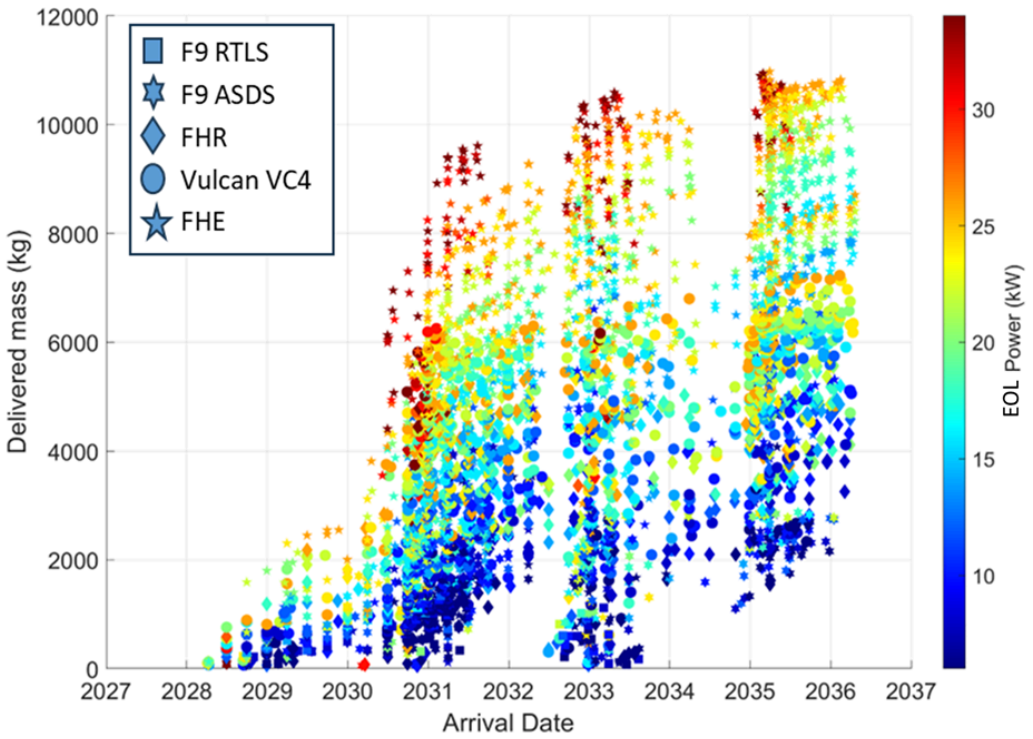



**Figure 4.6. Pareto-optimal solutions for rendezvous reconnaissance missions with launch no earlier than October 2027.**

**Table 4.3: Selected Rendezvous Reconnaissance Trajectory Options.**

| Case | Launch Date | Arrival Date | Flight Time (yrs) | Launch Vehicle | SEP EOL Power at 1 AU [kW] | Sequence | Delivered Mass (kg) | Approx. payload mass (kg) |
|---|---|---|---|---|---|---|---|---|
| 1 | 2027-10-01 | 2028-12-30 | 1.25 | FHE | 20 | Direct | 1801 | 10 |
| 2 | 2028-04-19 | 2030-04-19 | 2.00 | Vulcan VC4 | 18 | Direct | 2151 | 370 |
| 4 | 2028-08-18 | 2030-11-17 | 2.25 | FHE | 10 | EGA | 1990 | 300 |
| 5 | 2028-12-23 | 2030-09-22 | 1.75 | Vulcan VC4 | 18 | EGA | 1857 | 80 |
| 6 | 2029-03-31 | 2031-03-31 | 2.00 | Vulcan VC4 | 8 | Direct | 2062 | 390 |
| 7 | 2029-04-14 | 2031-01-12 | 1.75 | FHE | 20 | Direct | 3919 | 2110 |
| 8 | 2029-06-30 | 2031-03-31 | 1.75 | FHE | 20 | Direct | 2484 | 680 |
| 9 | 2029-06-30 | 2031-06-30 | 2.00 | Vulcan VC4 | 12 | Direct | 1879 | 160 |
| 10 | 2029-12-30 | 2032-09-28 | 2.75 | FHR | 12 | EGA | 1782 | 70 |
| 11 | 2029-12-31 | 2031-12-31 | 2.00 | FHE | 16 | VGA | 1911 | 150 |

The case 11 trajectory from Table 4.3 is plotted in Figure 4.7. This selected example for rendezvous reconnaissance launches on a Falcon Heavy Expendable LV and exploits a Venus gravity assist to change inclination and increase the spacecraft's semi-major axis. The spacecraft thrusts nearly continuously outside of an assumed 90% thruster duty cycle and forced coasts after launch and before the gravity assist.

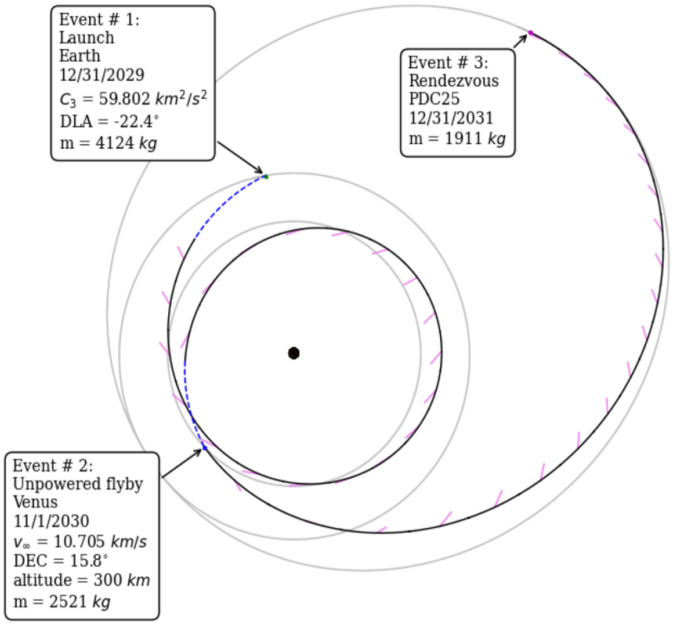



**Figure 4.7: Exemplar rendezvous reconnaissance trajectory based on a 16-kW SEP system and Falcon Heavy Expandable Launch.**

The rendezvous reconnaissance mission is required to determine the asteroid's mass, image the side not previously visible to the flyby spacecraft, and monitor the asteroid's state following any mitigation efforts. As in the flyby case, the short development time is the most stressing aspect of completing this mission, so we recommend a set of the fewest instruments sufficient to achieve these measurements. This set includes a narrow angle camera, a wide angle camera, a LiDAR, and radio science. The LiDAR's benefit to the mission is faster shape modeling, as demonstrated by the OSIRIS-REx mission at Bennu. LiDAR measurements don't depend on lighting and the shape modeling approach doesn't require multiple varied images of the same feature, as is the case with stereophotoclinometry. There exist multiple high-heritage instrument candidates for this scenario both in the U.S. and internationally.

## 5. Kinetic Impactor (KI) Mission Campaign Analysis

Kinetic impactor mission trajectory designs are combined with hydrocode modeling to refine KI designs and generate predictions of deflection performance, along with associated mission requirements.

*5.1 KI Mission Campaign Strategies*

A primary and backup launch period are assessed for KI missions, to provide robustness and redundancy, and to assess the consequences of delaying the deployment of deflection missions. For the Primary KI mission campaign, the earliest KI launch is no earlier than 2 years after Epoch 2 (i.e., KI missions launch no earlier than April 2030). As described previously, the RRS launches during December 2029 and rendezvouses with the asteroid during December 2031. To ensure that the asteroid is well characterized before the KIs begin striking the asteroid, and to ensure that the rendezvous spacecraft is on station to provide situational awareness throughout the KI strikes, the KI trajectories are constrained to impact the asteroid no earlier than 4 months after the RRS arrives at the asteroid (i.e., the KIs impact the asteroid no earlier than April 2032). The first several KI missions must be designed with several factors of uncertainty in asteroid mass that remains after the flyby reconnaissance at Epoch 2, as shown in Table 2.1.

For the Backup KI mission campaign, the earliest KI launch is 2 years and 4 months after the RRS arrives at the asteroid (i.e, KIs launch no earlier than April 2034). This allows knowledge of the asteroid's precise mass to be factored into the design of the KI spacecraft before launch, with the tradeoff of delaying the deflection of the asteroid.

For multi-KI campaigns, we enforce constraints of at least 10 days between launches and at least 14 days between kinetic impacts on the asteroid, to allow enough time for debris clearing and estimation of achieved ΔV and β.

*5.2 Spacecraft Trajectory Analysis*

The KI mission trajectories are generated by performing a grid scan of ballistic Earth to asteroid trajectories produced by solving Lambert's problem. The Lambert solutions test all combinations of short-way and long-way trajectory options and span multiple revolutions, where the number of revolutions is selected to be appropriate for the Time of Flight (TOF), also referred to as the L to D (launch to deflection time). All multi-revolution solutions consider both left branch and right branch solutions. For each point in the grid, the combination of Lambert solution parameters—short-way, long-way, number of revolutions, left branch, right branch—that maximizes the deflection of the asteroid in the B-plane is selected.

The amount by which the asteroid is deflected in the B-plane is calculated using the partial derivatives of the asteroid's B-plane coordinates with respect to the components of the ΔV vector. The ΔV vector is calculated from the standard equation for the ΔV imparted to an asteroid by a kinetic impactor, given in Eq. (5.1).

$$\Delta\vec{V} = \frac{\beta \vec{V_\infty} m_{KI}}{m_{asteroid}} \tag{5.1}$$

where β is the momentum enhancement factor, $\vec{V_\infty}$ is the velocity of the spacecraft relative to the asteroid upon striking the asteroid, $m_{KI}$ is the mass of the kinetic impactor spacecraft, and $m_{asteroid}$ is the mass of the asteroid. The momentum

enhancement factor describes how much the ejecta produced by the impact on the asteroid contributes to the overall change in the asteroid's momentum, and therefore the change in velocity. A β of 1 represents no contribution from ejecta, a β of 2 means the momentum of the ejecta equals the momentum of the spacecraft, and a β > 2 means the momentum of the ejecta exceeds the momentum of the spacecraft.

The results of the KI trajectory grid scan, in terms of how much the asteroid is deflected in the B-plane, are shown in Figure 5.1.

The trajectory solutions in Figure 5.1 are essentially unconstrained, apart from bounds on the launch date, TOF, and asteroid arrival date. Applying constraints on Earth departure $C_3$, Declination of the Launch Asymptote (DLA), Sun-Earth-Spacecraft (SES) angle, spacecraft speed relative to asteroid at impact, and approach phase angle at impact reduce the space of feasible trajectories, as shown in Figure 5.2.

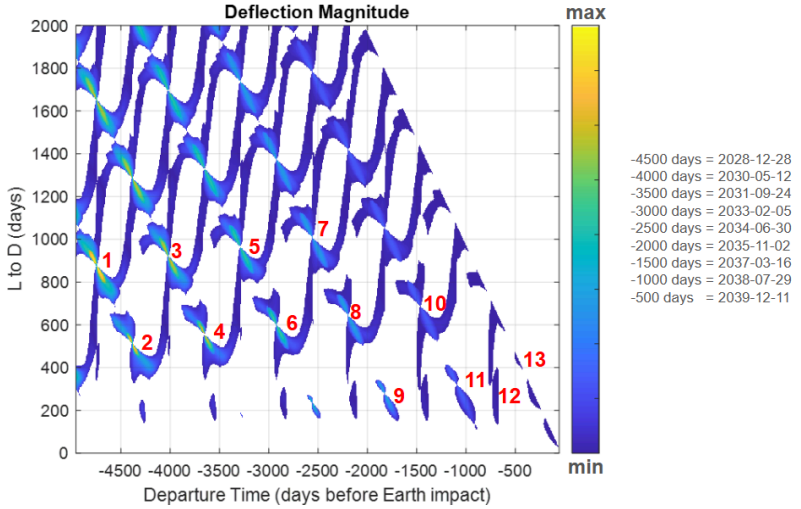



**Figure 5.1: Grid scan of KI trajectories with optimized Lambert solution parameters. The color scale shows the amount by which the asteroid is deflected in the B-plane, in a relative sense. Distinct families of trajectory solutions are marked with red numbers in chronological order from left to right.**

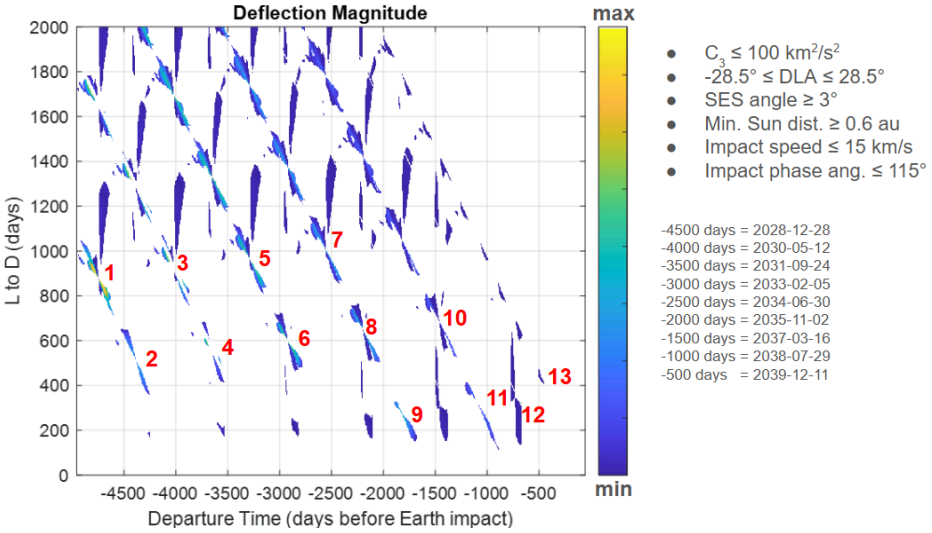



**Figure 5.2: Grid scan of KI trajectories with optimized Lambert solution parameters. The color scale shows the amount by which the asteroid is deflected in the B-plane, in a relative sense. The trajectory constraints listed in the figure are applied, reducing the space of feasible trajectories. Distinct families of trajectory solutions are marked with red numbers in chronological order from left to right.**

The upper limit on $C_3$ is the highest $C_3$ performance listed for the Falcon Heavy Expendable launch vehicle. The DLA limits correspond to a launch from the Cape Canaveral Space Force Station, and the launch mass versus $C_3$ performance curve used for the Falcon Heavy Expendable launch vehicle in this analysis is only valid within those DLA limits. The upper bound on the asteroid impact speed and the approach phase angle are both only notional.

Of the KI trajectory solutions capable of deflecting the asteroid fully off the Earth, the solution imparting minimum ΔV to the asteroid was selected, as this will minimize the likelihood of exceeding the asteroid fragmentation heuristic of ΔV ≤ 10% $V_{escape}$. As shown in Tables 5.1 and 5.2, a single KI would be sufficient to achieve total southward deflection of any realization of the asteroid mass for either the Primary or Backup launch dates. However, note that in all cases, the required deflection ΔV would exceed 10% $V_{escape}$ and thus risk fragmentation of the asteroid, according to our current heuristic. We therefore develop a strategy to use multiple KIs to achieve deflection while keeping each individual ΔV applied to the asteroid below the 10% $V_{escape}$ fragmentation threshold heuristic.

**Table 5.1. Minimum ΔV Single KI Deflection Options for the Primary Launch Period.**

| Asteroid Mass | Launch Date | TOF (d) | Arrival Date | $C_3$ ($km^2/s^2$) | Mass (kg) | Vrel (km/s) | β | ΔV (cm/s) | ΔV (%$V_{escape}$) |
|---|---|---|---|---|---|---|---|---|---|
| **Low Mass** | 2031-03-14 | 586 | 2032-10-20 | 22.774 | 1379 | 11.74 | 2 | 1.55 | 26% |
| **50th %tile Mass** | 2031-03-14 | 586 | 2032-10-20 | 22.774 | 1037 | 11.74 | 5 | 1.55 | 19% |
| **High Mass** | 2031-03-14 | 586 | 2032-10-20 | 22.774 | 1692 | 11.74 | 5 | 1.55 | 15% |

**Table 5.2. Minimum ΔV Single KI Deflection Options for the Backup Launch Period.**

| Asteroid Mass | Launch Date | TOF (d) | Arrival Date | $C_3$ ($km^2/s^2$) | Mass (kg) | Vrel (km/s) | β | ΔV (cm/s) | ΔV (%$V_{escape}$) |
|---|---|---|---|---|---|---|---|---|---|
| **Low Mass** | 2034-05-09 | 222 | 2034-12-17 | 34.486 | 1501 | 13 | 2 | 1.87 | 31% |
| **50th %tile Mass** | 2034-05-09 | 222 | 2034-12-17 | 34.486 | 1129 | 13 | 5 | 1.87 | 22% |
| **High Mass** | 2034-05-09 | 222 | 2034-12-17 | 34.486 | 1841 | 13 | 5 | 1.87 | 18% |

*5.3 KI Modeling for β Prediction*

Our strategy for being able to launch at least some of the KIs before the asteroid mass is measured by the rendezvous reconnaissance mission, and before the β behavior is observed, is to size the KIs to impart a ΔV with ~4% $V_{escape}$ for the Low Mass realization of the asteroid at an assumed β of 2, thereby avoiding fragmentation risk even if β is up to ~5. This results in a KI mass of 200 kg and an impact speed of 12.37 km/s. For a direct comparison, such an impactor has about 33% less momentum than DART but about 33% more kinetic energy. The performance of our KI design against all three realizations of the asteroid (Low, 50th Percentile, and High Mass) was assessed, using multiple plausible crush curves and rubble pile vs. regolith vs. monolithic structures with an appropriate ellipsoidal asteroid shape, as shown in Figure 5.3.

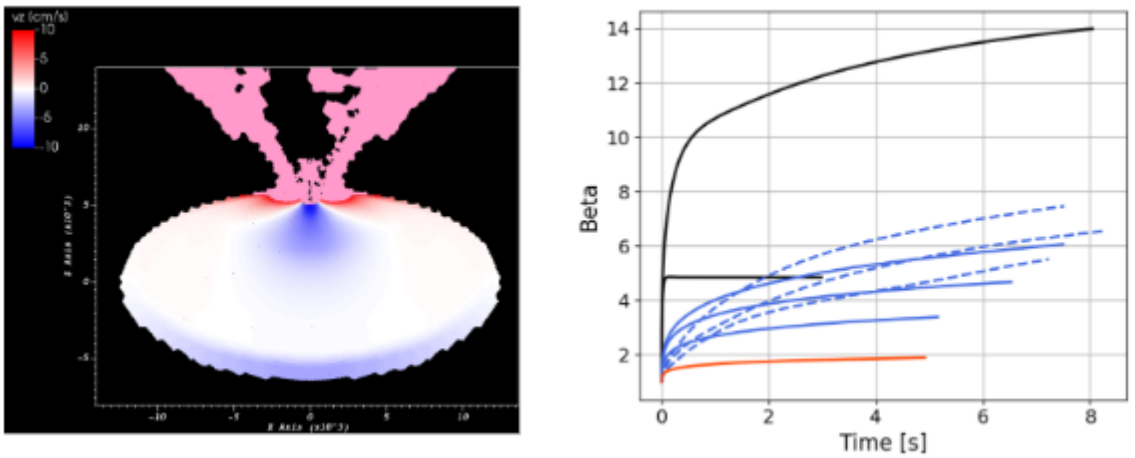



**Figure 5.3: Left: Exemplar KI simulation vs. the Epoch 2 asteroid properties. Right: β results for Low Mass asteroid (red), 50th Percentile asteroid (blue - solid lines are different crush curves for regolith, dashed lines are rubble pile realizations w/ Dimorphos-like crush curve), and High mass asteroid (black - higher β for Chelyabinsk meteorite-like (weak) damage model, lower β for Abu Panu meteorite-like (strong) damage model).**

To simulate the kinetic impact and understand the possible ranges for β, we use Spheral++, a smoothed particle hydrodynamics (SPH) code tailored for shock and impact physics and maintained by Lawrence Livermore National Laboratory [15,16,17], and FLAG, a finite-volume arbitrary Lagrangian–Eulerian (ALE) code developed and maintained by Los Alamos National Laboratory [18,19,20]. In our

Spheral++ simulations, we include models for elastoplasticity, fracture, microporosity, and N-body gravity. Our strength and fracture implementations are largely based on the work of Benz and Asphaug [21], who implemented an elastic perfectly-plastic strength model and a probabilistic approach to fracture [22] in SPH.

We use a pressure-dependent yield-strength model based on the work of Collins et al. [23] with separate functional forms for intact and damaged material. To model porosity, Spheral++ provides the option to use either the P-alpha model [24,25] or the epsilon-alpha model [26,23]. To examine the sensitivity of our impact calculations to the porosity model, we vary the porosity model as well as the crush curve used by the P-alpha model. Stickle [27] noted the sensitivity of impact calculation to the specifics of the porosity model. Our FLAG simulations use constitutive models, damage models, microporosity via the P-α model [24], and a new capability for a gravity monopole [20]. FLAG has been used extensively in multi-physics regimes and has been verified and validated against theoretical and laboratory data for metals and geologic materials at both solid and porous densities [28,29,30,31,32,33,34,35].

In our Spheral++ simulations, we use three different materials to describe our system. The impactor is modeled as a single aluminum sphere while the asteroid is treated as a heterogeneous mixture of explicitly resolved boulders and regolith. Regolith represents all sub-resolution-scale cobbles, pebbles, and fines. For the aluminum impactor, we use a tabulated equation of state from the Livermore Equation of State (LEOS) library [36]. For the asteroidal material, we use an M-ANEOS model of dunite [37]. Boulders and regolith are initialized with different porosities and regolith is initialized as fully damaged. The impactor is discretized uniformly with 5-cm particles according to the approach of Raskin and Owen [38]. The impact site on the asteroid is likewise discretized at 5-cm resolution but is then graded away from the impact site for computational expediency. The general approach outlined in this section has been previously used to model the DART impact [30,27].

In our FLAG simulations, we used a tabular equation of state from the SESAME database [39] for both the Al-6061 impactor and the porous basalt target. The surrounding material was modeled as void. We ran 2D and 3D Cartesian simulations of an ellipsoidal target being struck by an aluminum sphere. We varied the resolution of the computational mesh to include zone sizes in the meter to centimeter range, depending on proximity to the point of impact. FLAG simulations covered the parameter space of Epoch 2 data, from solid rock to porous rock, with equivalent porosities to match the given bulk densities. We modeled the highest mass asteroid as intact rock. The bulk density of this realization (3.372 g/cm$^3$) is larger than the base density of forsterite (3.32 g/cm$^3$), so we scaled the size of the asteroid such that the total mass would match Table 2.1, assuming no porosity. The key variable we explored for this realization was the damage model, representing how easily material could be fractured. We compared a damage model calibrated to experiments on Chelyabinsk material [40] and one calibrated to experiments on Aba Panu [41]. Chelyabinsk material fractures more easily than Aba Panu, leading to a larger damage extent and therefore a higher β.

The median asteroid, with a bulk density of 2.207 g/cm$^3$, was modeled as either a homogeneous regolith body or as a rubble pile composed of boulders interspersed

with porous regolith. For the homogeneous regolith body, we examined the effect of changing the crush curve between a P-alpha model approximating lunar regolith [42], a P-alpha model used by Raducan et al. [43] to model a Dimorphos-like asteroid, and an epsilon-alpha model similar to that used by Stickle et al. [27] to model the DART impact. The differences between these crush curves change β by up to ~2.5, demonstrating the importance of understanding the behavior of compacting material for predicting a porous asteroid's response. For the rubble pile simulations, we kept the crush curve constant, using the parameters utilized in Raducan et al. [43]. We created three different arrangements of boulders, filling 50% of the median asteroid with boulders ranging from 2 m in radius to 20 m in radius. These three random arrangements showed β values that varied by ~2, depending on whether the impactor struck regolith or a boulder, and at what angle.

We performed a single simulation on the lowest mass asteroid, which has a bulk density of 1.128 g/cm$^3$. To simplify comparisons across the three asteroid sizes, we model this asteroid as a homogeneous regolith body using the same epsilon-alpha crush curve as for the median homogeneous regolith asteroid. The extremely high porosity of the lowest mass asteroid dampens β compared to the other simulations as more impact energy is used in compaction rather than ejection of material.

While our β values reach higher than the 2-5 originally planned for in the mission design, our 200-kg KI does not appear to pose fragmentation risk to any realization of the asteroid (Low, 50th Percentile, or High Mass) across the cases modeled and the ranges of β observed in those models. A β of ~5 represents the median behavior of the full dataset, but higher kinetic energy and lower asteroid bulk porosity tend to produce higher values of β. Therefore, β could be larger than 5 for the 50th Percentile and High Mass asteroids. Meanwhile, β may be lower, e.g., ~2, for the Low Mass asteroid due to its higher porosity. To account for the uncertainties in both β and asteroid mass, we will show KI deflection mission campaign design results for β values of 2, 5, and 8 across the three asteroid realizations (Low, 50th Percentile, and High Mass).

### *5.4 KI Mission Options Results*

The grid of KI trajectories compliant with all of the aforementioned constraints were rank-ordered according to the amount of asteroid deflection in the B-plane achieved by each. Sets of KI trajectories capable of achieving total deflection of the asteroid off the Earth were then selected within the bounds of the Primary KI campaign launch period and within the bounds of the Backup KI campaign. The resulting sets of trajectories are detailed in Tables 5.3 and 5.4.

**Table 5.3. KI Trajectories for Primary Launch Period Campaign.**

| | Launch Date | TOF (days) | Arrival Date | $C_3$ ($km^2/s^2$) | DLA (deg) | Vrel (km/s) | SES Angle (deg) | Approach Phase Angle (deg) | Short-Way or Long-Way | Number of Revs | Left Branch or Right Branch |
|---|---|---|---|---|---|---|---|---|---|---|---|
| 1 | 2030-07-17 | 866 | 2032-11-29 | 28.678 | -27 | 10.88 | 3.02 | 110.22 | Long-Way | 2 | Left Branch |
| 2 | 2031-02-16 | 598 | 2032-10-06 | 49.155 | -9.4 | 12.37 | 4.54 | 72.37 | Short-Way | 2 | Right Branch |
| 3 | 2031-03-14 | 586 | 2032-10-20 | 22.774 | -8.63 | 11.74 | 3.19 | 82.9 | Short-Way | 2 | Right Branch |
| 4 | 2034-05-09 | 222 | 2034-12-17 | 34.486 | 7.49 | 13 | 24.27 | 84.67 | Long-Way | 0 | N/A |
| 5 | 2035-01-12 | 704 | 2036-12-16 | 54.803 | -12.96 | 11.38 | 51.04 | 53.37 | Short-Way | 2 | Right Branch |
| 6 | 2035-01-28 | 702 | 2036-12-30 | 26.064 | -17.36 | 10.66 | 49.71 | 63.51 | Short-Way | 2 | Right Branch |

**Table 5.4. KI Trajectories for Backup Launch Period Campaign.**

| | Launch Date | TOF (days) | Arrival Date | $C_3$ ($km^2/s^2$) | DLA (deg) | Vrel (km/s) | SES Angle (deg) | Approach Phase Angle (deg) | Short-Way or Long-Way | Number of Revs | Left Branch or Right Branch |
|---|---|---|---|---|---|---|---|---|---|---|---|
| 1 | 2034-05-09 | 222 | 2034-12-17 | 34.486 | 7.49 | 13 | 24.27 | 84.67 | Long-Way | 0 | N/A |
| 2 | 2035-01-12 | 704 | 2036-12-16 | 54.803 | -12.96 | 11.38 | 51.04 | 53.37 | Short-Way | 2 | Right Branch |
| 3 | 2035-01-28 | 702 | 2036-12-30 | 26.064 | -17.36 | 10.66 | 49.71 | 63.51 | Short-Way | 2 | Right Branch |
| 4 | 2035-02-25 | 688 | 2037-01-13 | 9.945 | -21.08 | 10.24 | 48.28 | 75.83 | Short-Way | 2 | Right Branch |
| 5 | 2035-06-25 | 596 | 2037-02-10 | 8.722 | -27.98 | 10.01 | 46.62 | 98.18 | Long-Way | 1 | Left Branch |
| 6 | 2035-08-14 | 560 | 2037-02-24 | 21.708 | -28.47 | 9.03 | 46.91 | 107.33 | Long-Way | 1 | Left Branch |

The first two KI trajectories for the Primary launch period listed in Table 5.3 are plotted in Figure 5.4, for reference. The other KI trajectories for the Primary and Backup launch periods listed in Tables 5.3 and 5.4 are of similar character.

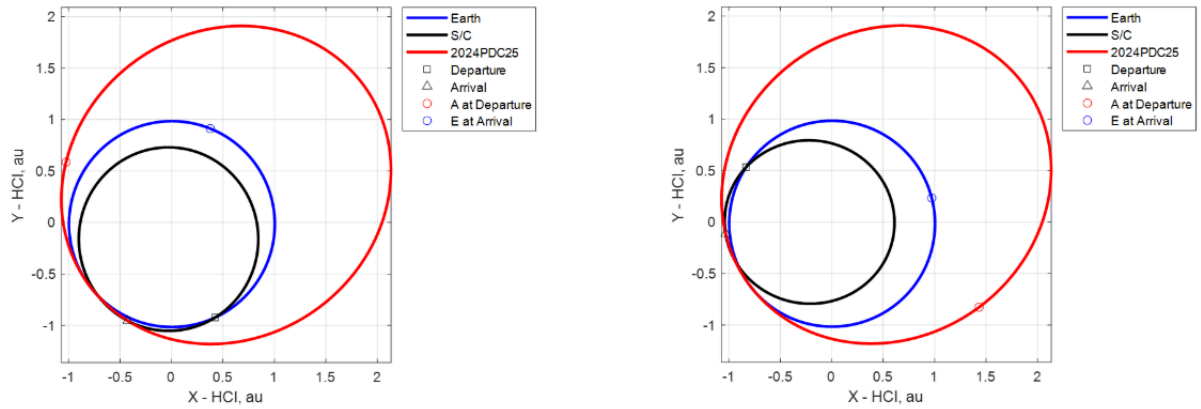



**Figure 5.4. KI trajectories 1 (left) and 2 (right) for the Primary Launch Period campaign. The other KI trajectories in the Primary and Backup Launch Periods are of similar character.**

The Primary and Backup launch period KI trajectories were applied to each of the three values of asteroid mass, and for each of the three reference β values mentioned previously: 2, 5, and 8 (but omitting the β = 8 case for the Low Mass asteroid, because modeling indicated that a β that high with such a low asteroid porosity is highly unlikely). A summary of the timeline of KI missions within the Primary campaign and the associated progression of the asteroid's deflection is shown in Figure 5.5.

**1. Launch 2031-02-16**
**m = 200 kg, v = 12.37 km/s**

| Deflection Date | β | | |
|---|---|---|---|
| 2032-10-06 | | | |
| Asteroid Mass | 2 | 5 | 8 |
| Low Mass | 15% | 37% | |
| 50th %tile | 8% | 20% | 32% |
| High Mass | 5% | 12% | 19% |

**2. Launch 2031-03-14**
**m = 200 kg, v = 11.74 km/s**

| Deflection Date | β | | |
|---|---|---|---|
| 2032-10-20 | | | |
| Asteroid Mass | 2 | 5 | 8 |
| Low Mass | 14% | 36% | |
| 50th %tile | 8% | 19% | 31% |
| High Mass | 5% | 12% | 19% |

| Cumulative - 2032-10-20 | | | |
|---|---|---|---|
| | β | | |
| Asteroid Mass | 2 | 5 | 8 |
| Low Mass | 29% | 73% | |
| 50th %tile | 16% | 39% | 62% |
| High Mass | 10% | 24% | 38% |

**3. Launch 2030-07-17**
**m = 200 kg, v = 10.88 km/s**

| Deflection Date | β | | |
|---|---|---|---|
| 2032-11-29 | | | |
| Asteroid Mass | 2 | 5 | 8 |
| Low Mass | 12% | 31% | |
| 50th %tile | 7% | 17% | 27% |
| High Mass | 4% | 10% | 16% |

| Cumulative - 2032-11-29 | | | |
|---|---|---|---|
| | β | | |
| Asteroid Mass | 2 | 5 | 8 |
| Low Mass | 42% | 105% | |
| 50th %tile | 22% | 56% | 89% |
| High Mass | 14% | 34% | 55% |

**4. Launch 2034-05-09**
**m = 194–2606 kg, v = 13.0 km/s**

| Deflection Date | β | | |
|---|---|---|---|
| 2034-12-17 | | | |
| Asteroid Mass | 2 | 5 | 8 |
| Low Mass | 32% | 32% | |
| 50th %tile | 44% | 44% | 44% |
| High Mass | 56% | 56% | 56% |

| Cumulative - 2034-12-17 | | | |
|---|---|---|---|
| | β | | |
| Asteroid Mass | 2 | 5 | 8 |
| Low Mass | 74% | 137% | |
| 50th %tile | 67% | 100% | 134% |
| High Mass | 70% | 91% | 111% |

**5. Launch 2035-01-12**
**m = 222–2977 kg, v = 11.38 km/s**

| Deflection Date | β | | |
|---|---|---|---|
| 2036-12-16 | | | |
| Asteroid Mass | 2 | 5 | 8 |
| Low Mass | 17% | 17% | |
| 50th %tile | 24% | 24% | 24% |
| High Mass | 30% | 30% | 30% |

| Cumulative - 2036-12-16 | | | |
|---|---|---|---|
| | β | | |
| Asteroid Mass | 2 | 5 | 8 |
| Low Mass | 91% | 154% | |
| 50th %tile | 90% | 124% | 157% |
| High Mass | 100% | 120% | 141% |

**6. Launch 2035-01-28**
**m = 237–3178 kg, v = 10.66 km/s**

| Deflection Date | β | | |
|---|---|---|---|
| 2036-12-30 | | | |
| Asteroid Mass | 2 | 5 | 8 |
| Low Mass | 18% | 18% | |
| 50th %tile | 24% | 24% | 24% |
| High Mass | 31% | 31% | 31% |

| Cumulative - 2036-12-30 | | | |
|---|---|---|---|
| | β | | |
| Asteroid Mass | 2 | 5 | 8 |
| Low Mass | 109% | 172% | |
| 50th %tile | 115% | 148% | 181% |
| High Mass | 131% | 151% | 172% |

**Figure 5.5. Timeline of KI missions for the Primary Launch Period and their individual and cumulative asteroid deflection performances.**

In the Primary KI campaign, the first three KIs are the 200 kg KIs discussed previously, for which modeling results do not show risk of asteroid fragmentation. The fourth, fifth, and sixth KIs have masses that are tailored after the RRS provides a precise measurement of the asteroid's mass. The β behavior is assumed to be the same across impacts, making it predictable after observing the first KI's impact on the asteroid. Six KIs are able to complete the deflection of the asteroid even if β is low, and fewer KIs (3–5) may be needed if β is moderate or high.

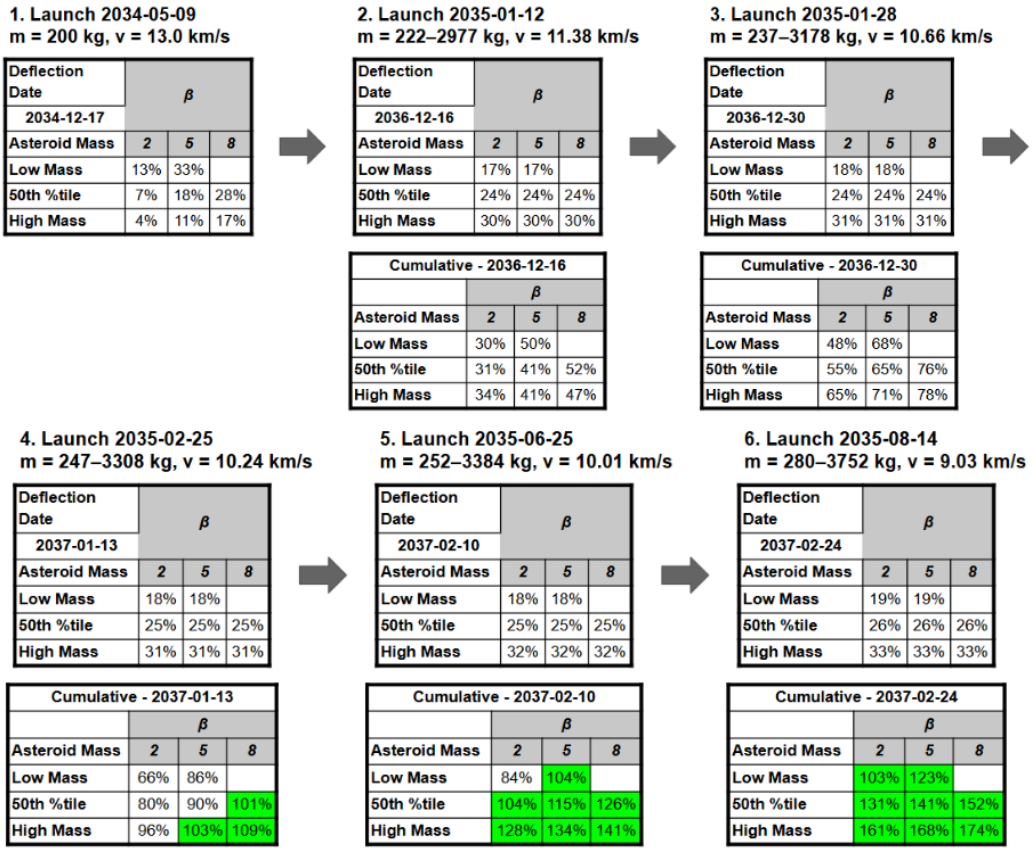



**Figure 5.6. Timeline of KI missions for the Backup Launch Period and their individual and cumulative asteroid deflection performances.**

A summary of the timeline of KI missions within the Primary campaign and the associated progression of the asteroid's deflection is shown in Figure 5.6. In the Backup KI campaign, the first KI is the 200 kg that does not appear to pose an asteroid fragmentation risk. The remainder of the KIs all launch after the RRS has precisely measured the asteroid's mass, and after the first KI shows the behavior of β, which is assumed to be constant across KI impacts on the asteroid. Therefore, KIs 2 through 6 can have their masses tailored to be maximally effective against the asteroid while keeping each ΔV imparted to the asteroid below the fragmentation threshold heuristic.

Table 5.5 summarizes the number of KI spacecraft required and deflection completion date for each combination of asteroid mass and β for the Primary KI

campaign, with the more likely combinations of asteroid mass and β highlighted in light green. Table 5.6 provides the same information for the Backup KI campaign.

**Table 5.5: Number of KI spacecraft required to completely deflect the asteroid, and the associated deflection completion date, for the Primary KI campaign.**

| Primary: Number of KI Spacecraft Required to Complete Deflection & Completion Date | | | |
|---|---|---|---|
| | | | |
| **Asteroid Mass** | **2** | **5** | **8** |
| **Low Mass** | 6<br>Dec 2036 | 3<br>Nov 2032 | |
| **50th %tile** | 6<br>Dec 2036 | 4<br>Dec 2034 | 4<br>Dec 2034 |
| **High Mass** | 5<br>Dec 2036 | 5<br>Dec 2036 | 4<br>Dec 2034 |

**Table 5.6: Number of KI spacecraft required to completely deflect the asteroid, and the associated deflection completion date, for the Backup KI campaign.**

| Backup: Number of KI Spacecraft Required to Complete Deflection & Completion Date | | | |
|---|---|---|---|
| | | | |
| **Asteroid Mass** | **2** | **5** | **8** |
| **Low Mass** | 6<br>Feb 2037 | 5<br>Feb 2037 | |
| **50th %tile** | 5<br>Feb 2037 | 5<br>Feb 2037 | 4<br>Jan 2037 |
| **High Mass** | 5<br>Feb 2037 | 4<br>Jan 2037 | 4<br>Jan 2037 |

Overall, both the Primary and Backup KI campaign require up to 6 KI spacecraft, despite the Backup KI campaign waiting to launch until after the RRS has precisely measured the asteroid's mass. This is because the first three KIs in the Primary campaign are launched before the RRS has measured the asteroid's mass and so are deliberately made small to avoid fragmentation risks, while only the first KI in the Backup campaign is made small and the remainder have masses tailored to the measured asteroid mass and observed β behavior.

Finally, while constant β across KI impacts on the asteroid was assumed for simplicity and for lack of information to the contrary, it is important to note that neither simulation capabilities nor flight test missions have afforded us the opportunity to investigate how β may change between subsequent impacts. For our mission design, we have assumed a constant value of β across all subsequent impacts, but as shown by the variation amongst the rubble-pile simulations for the median asteroid, β may vary significantly depending on impact location and impact processing from previous strikes. In the future, as simulation capabilities improve to the point that we can run models to late enough times such that they reach a post-impact equilibrium, we intend to address these uncertainties.

## 6. Ion Beam Deflection (IBD) Mission Campaign Analysis

### *6.1 Methodology*

Ion-Beam Deflection (IBD) is a method for changing the orbit of an asteroid by directing the exhaust beam of an ion engine onto its surface. It involves rendezvousing a high-power Solar Electric Propulsion (SEP) spacecraft with the asteroid, establishing a position roughly 3-4 asteroid diameters from the surface and firing an opposing pair of ion thrusters so that most of the beam from one of the thrusters impinges onto the asteroid. The momentum of the impinging ions is imparted to the asteroid while the spacecraft is kept on-station by the symmetric firing of an opposing thruster (Figure 6.1). The ions in the beam move at very high velocities, and over time, they can impart a considerable amount of momentum to the asteroid. The impinging ions are effectively absorbed by the asteroid surface; residual sputtering will be at very low velocity, producing negligible momentum enhancement. Provided the spacecraft can maintain its station, the momentum imparted to the asteroid is highly predictable and does not depend on asteroid physical properties.

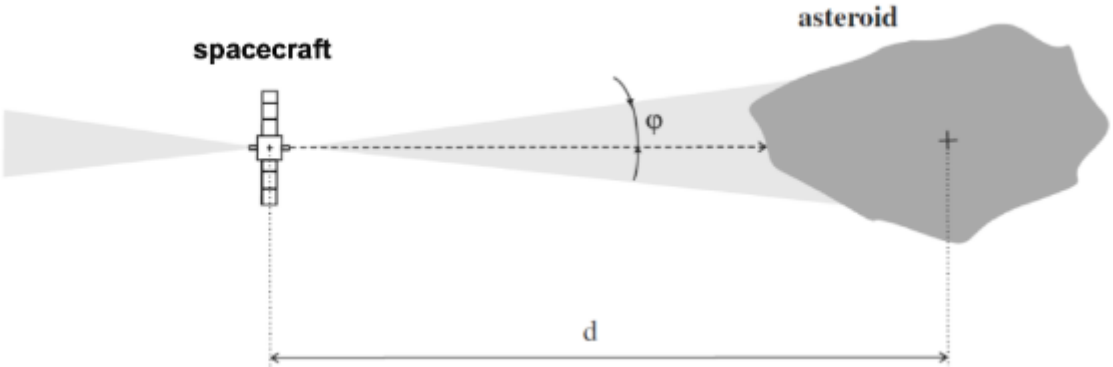



**Figure 6.1. Conceptual drawing of IBD spacecraft positioning relative to the asteroid during operations Angle φ is the beam divergence.**

When analyses of IBD performance for the 2024 PDC25 case were first started, a large number of mission designs were considered, with a wide variety of assumed launch dates, arrival dates, power levels, numbers of ion thrusters, and propellant loads. A preliminary set of ion-beam deflection simulations were run to assess the relative performance of these missions. The key factors that led to the best

outcomes were: early arrival (preferably around the 2031-32 perihelion), spacecraft total available power, number of thruster pairs, and amount of propellant available for deflection. Our objective was to find a good balance among these factors that was also a realizable size of mission. In our IBD analyses at Epoch 1 of this scenario we highlighted an IBD Option A mission which had the very modest power level of 22 kW at 1 AU, modeled after the power level of the Psyche spacecraft. That mission alone could successfully deflect roughly 60% of the possible combinations of asteroid size and impact locations at Epoch 1. But it was underpowered: the spacecraft could not power the thrusters through much of the asteroid orbit. Increasing the spacecraft power to 46 kW achieved a much better balance since it could make better use of the same 6-NEXT-C thruster set assumed for Option A to deliver considerably more deflection.

For Epoch 2, we settled on a purpose-built 46-kW IBD spacecraft and considered it to be already under development. We also considered a second IBD spacecraft design based on a repurposed 60-kW component of Lunar Gateway. The optimal rendezvous trajectory designs and deflection performance for both of these IBD spacecraft models are described in the following sections.

*6.2 Spacecraft Trajectory Analysis*

A high-power SEP system has multiplicative advantages for IBD. Higher power enables more thrusters and higher mass flow rates during periapsis passage when it is most effective to change the asteroid's orbit. Additionally, high-power SEP systems can reduce the flight time for a rendezvous trajectory to the asteroid, allowing for earlier arrival dates and potentially access to deflection during earlier perihelion passages. The starting time for deflection operations is important, as the earlier perihelion passages provide higher effective deflection per unit mass of propellant. Moreover, higher SEP power generally correlates with higher delivered mass capability, allowing for increased propellant available for IBD operations.

A capable high-power SEP system with high-capacity xenon tanks was developed for the NASA Asteroid Redirect Robotic Mission (ARRM), which was cancelled in 2017. The ARRM spacecraft design included a 46-kW-class solar array, four ~14-kW thrusters, and up to 5000 kg of xenon propellant. The ARRM SEP spacecraft design with replacement of the four baseline thrusters with six NEXT-C thrusters provides a capable SEP spacecraft for IBD operations. This purpose-built spacecraft for IBD is designed with the NEXT-C thrusters pointed in opposing direction pairs. As such, only three thrusters are assumed to be active for the transfer trajectory, while all six thrusters will be active during IBD operations.

To determine candidate rendezvous trajectories, optimal trajectories were developed with the goal of maximizing delivered mass, maximizing launch date, and minimizing arrival date. Launch dates between January 2029 and January 2032 are traded, and the arrival date is constrained to be before the November 2032 perihelion. A Falcon Heavy Expendable launch vehicle is assumed for all trajectories given the need for large xenon mass delivered. The arrival date versus launch date for the resulting Pareto-optimal trajectories are plotted in Figure 6.2 with the color indicating the estimated xenon available for IBD operations after arrival. The highest performing rendezvous solutions launch in early- to mid-2029 with up 5000 kg of xenon

available for IBD operations for June 2032 arrival dates. However, this family of solutions does not allow for the desired period of at least five years from ATP to launch. An alternative family of solutions launches around October 2029, five years after ATP, and provides up to 2700 kg of xenon for IBD, depending on the selected arrival date. Later launch dates are also available, but only with later arrival date potential and generally reduced delivered xenon for IBD operations.

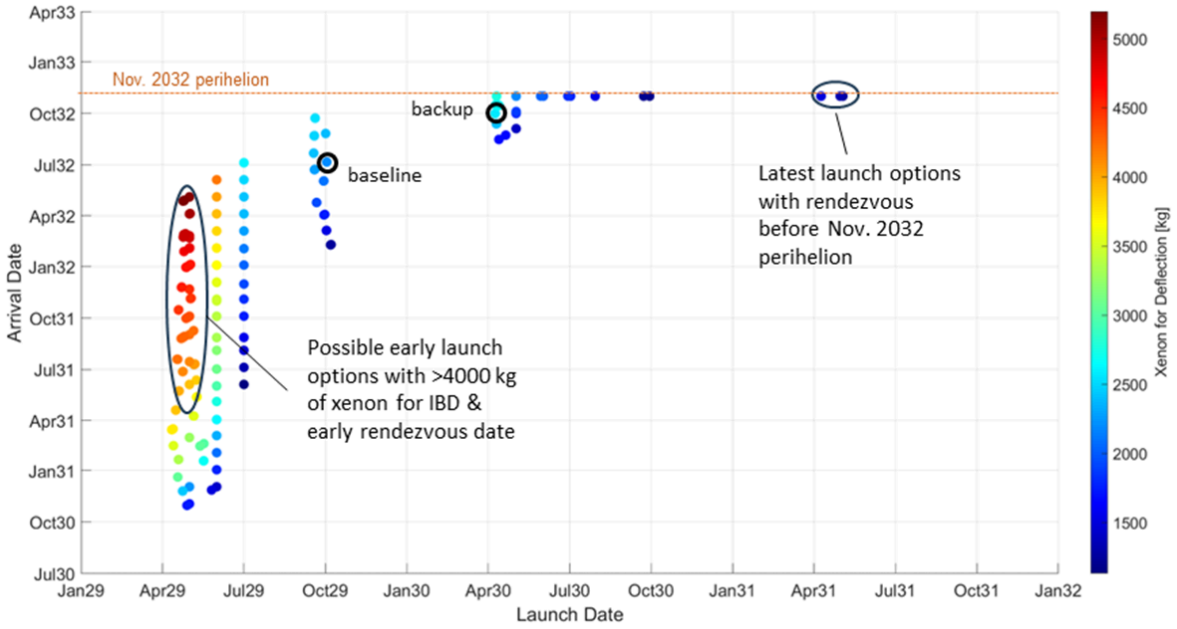



**Figure 6.2. Pareto-optimal solution space for rendezvousing with 2024 PDC25 with purpose-built 46-kW SEP system for IBD.**

Selected rendezvous trajectory options based on the optimal solution space are outlined in Table 6.1. Two early launch options follow direct, three-year trajectories to the asteroid, and offer high delivered xenon loads. The key drawback of these early options is that the launch dates only allow for 4.5 years of development after ATP. The primary rendezvous trajectory option allows for a five year development, and leverages a Venus gravity assist (VGA) to deliver roughly 2,200 kg of xenon for IBD operations. The trajectory plot for the primary option is shown in Figure 6.3. Finally, the backup option allows for a 5.5-year development timeline from ATP, launching in April 2030 and arriving roughly one month before the 2032 perihelion.

**Table 6.1. Rendezvous Trajectory Options for IBD Based on Purpose-Built 46-kW SEP Spacecraft.**

| Case | Launch Date | Arrival Date | Time of Flight [years] | Launch Mass [kg] | Delivered Mass to Asteroid [kg] | Xenon for Trajectory from Earth to Asteroid [kg] | Estimated Xenon for IBD ops [kg] | Total Estimated Xenon [kg] | Flyby sequence |
|---|---|---|---|---|---|---|---|---|---|
| Early1 | 2029-04-25 | 2032-04-27 | 3.01 | 10295 | 8863 | 1432 | 5199 | 6631 | Direct |
| Early2 | 2029-06-02 | 2032-06-04 | 3.01 | 9235 | 7855 | 1380 | 4191 | 5571 | Direct |
| Primary | 2029-10-03 | 2032-07-06 | 2.76 | 7399 | 5867 | 1532 | 2203 | 3735 | VGA |
| Backup | 2030-04-10 | 2032-10-01 | 2.48 | 6949 | 6239 | 710 | 2575 | 3285 | direct |

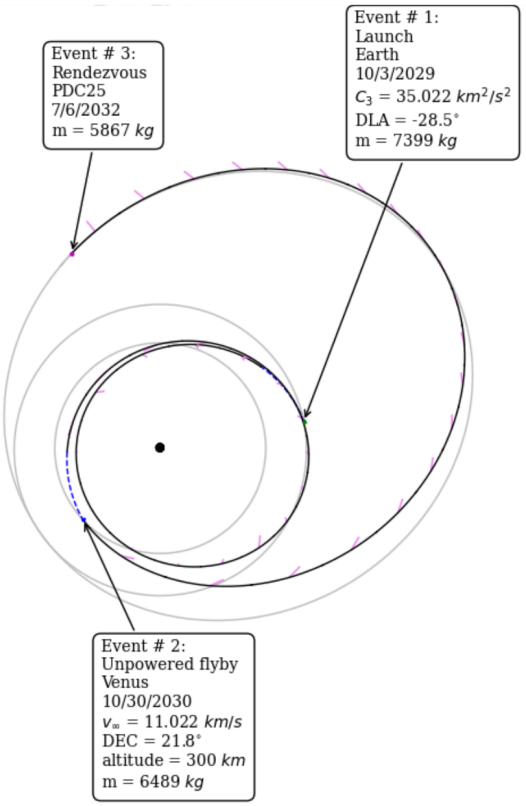



**Figure 6.3. Plot of primary rendezvous trajectory for IBD with a purpose-built 46 kW SEP system and NEXT-C thrusters.**

As an alternative to a purpose-built SEP system for IBD, repurposing or replicating the Power and Propulsion Element (PPE) being built for NASA's lunar Gateway is considered. The PPE spacecraft is a 60-kW SEP system planned for launch to cis-lunar space in 2027. The PPE spacecraft is composed of three 12-kW Advanced Electric Propulsion System (AEPS) thrusters and four 6-kW BHT-6000 thrusters. For the PPE to execute ion beam deflection, the BHT-6000 thrusters are moved to the opposite side of the spacecraft and reoriented to point in an opposing direction to the AEPS thrusters. During IBD operations, the AEPS thrusters point at the asteroid and the BHT-6000 thrusters provide countering thrust to maintain the hovering orbit. A drawback of applying the AEPS thrusters for IBD compared to NEXT-C thrusters is

the higher beam divergence angle, which contributes to a higher cosine loss in IBD performance. Additionally, the PPE spacecraft would need to be modified with larger xenon propellant tanks to accommodate the higher xenon loads for transferring to the asteroid and IBD operations.

For rendezvousing with the asteroid, it is assumed that only the three AEPS thrusters are applied for the transfer from Earth and the BHT-6000 thrusters are not active. As with the 46-kW purpose-built spacecraft, optimal rendezvous trajectories for the repurposed 60-kW PPE are identified via a many-objective optimization approach with the objective of maximizing launch date, minimizing arrival date, and maximizing delivered mass. The resulting solution space is similar to that of the 46-kW purpose-built spacecraft trajectories. Four selected options for the repurposed 60-kW PPE spacecraft are listed in Table 6.2. In comparison to the selected options for the purpose-built 46-kW spacecraft, the two early options in Table 6.1 do not provide as much xenon for IBD. However, the primary and backup options for the repurposed PPE deliver over 1,000 kg more xenon for IBD.

**Table 6.2. Rendezvous Trajectory Options for IBD Based on Repurposed 60-kW PPE Spacecraft.**

| Case | Launch Date | Arrival Date | Time of Flight [years] | Launch Mass [kg] | Delivered Mass to Asteroid [kg] | Xenon for Trajectory from Earth to Asteroid [kg] | Estimated Xenon for IBD ops [kg] | Total Estimated Xenon [kg] | Flyby sequence |
|---|---|---|---|---|---|---|---|---|---|
| Early1 | 2029-04-14 | 2032-03-16 | 2.92 | 13296 | 10050 | 3246 | 3772 | 7018 | Direct |
| Early2 | 2029-06-02 | 2032-05-04 | 2.92 | 12925 | 9480 | 3445 | 3203 | 6648 | Direct |
| Primary | 2029-10-02 | 2032-07-26 | 2.81 | 11625 | 8394 | 3231 | 2123 | 5354 | Venus |
| Backup | 2030-04-03 | 2032-10-31 | 2.58 | 13321 | 9494 | 3827 | 3218 | 6483 | Earth |

*6.3 IBD Modeling*

The performance of the various ion-beam missions and spacecraft models we considered was assessed via realistic simulations. At the heart of the simulations were the performance curves for the thrusters, basically giving thrust and propellant usage as a function of thruster input power. For the purpose-built IBD spacecraft we used NEXT-C performance curves, while for the repurposed PPE we used the AEPS and BHT performance curves. Each thruster had a maximum power and would be turned off when below its minimum power.

The main inputs to each IBD simulation were: start date, total spacecraft power at 1 AU, number of thruster pairs, and available propellant load. For the purpose-built IBD spacecraft the power was set at 46 kW and the number of thruster pairs was set at 3, but the other two inputs varied from mission to mission. The deflection start date was assumed to be one month after arrival. The deflection simulation proceeded incrementally on a day-by-day basis. The heliocentric distance on each day was used to compute the available power, and that was then reduced by 10% for

overhead and used to determine the number of thruster pairs that could operate. Thruster pairs would be turned off if not enough power was available for that pair. After that, the total thrust and propellant usage for that day was then computed using the thruster curves.

A fraction, nominally 95%, of the thrust from one thruster beam of each operating pair was assumed to be transferred to the asteroid. Basically, the spacecraft was assumed to be positioned at a distance from the asteroid that would maintain that impingement fraction. The positioning was also assumed to be in a direction that imparted ΔV would optimize the zeta component of deflection in the impact B-plane. The mass of the asteroid was then used to compute the imparted momentum into the ΔV vector for that day, and the deflection partial derivatives then used to map that ΔV vector into an incremental change in the asteroid's B-plane position. Figure 6.4 shows the relative daily contribution to B-plane deflection that could be achieved for these simulations, as a function of time. Note that the spacecraft in this simulation has enough power to deflect all the way around the orbit, right through aphelion. No scale is given on the vertical axis because the scale depends on the mass of the asteroid. Deflection capability peaks around each perihelion of the asteroid for two reasons: 1) that's when the power levels peak for the thrusters, resulting in peak thrust; and 2) that's when a given amount of ΔV produces the largest deflection in the B-plane.

To determine the optimal thrusting periods, an optimizer was used to select those days which could maximize the total accumulated b-plane displacement while attempting to reach the required deflection goal at the earliest completion date, with the additional constraint that there was still available propellant. Periods around the perihelia were clearly the most effective times to thrust. The total deflection of a given mission is essentially the integral under the curve in Figure 6.4, over the chosen thrusting arcs. The shaded region shows an example for one of the selected IBD missions. In this case, the thrusting began one month after arrival and ran continuously until the required deflection was achieved. In other more stressing cases, the optimizer would break the thrusting periods into arcs around two or more of the peaks in order to use propellant more judiciously. If the simulation determined that the accumulated B-plane deflection could not reach the required goal with the available propellant, it would add another copy of the spacecraft, and run again.

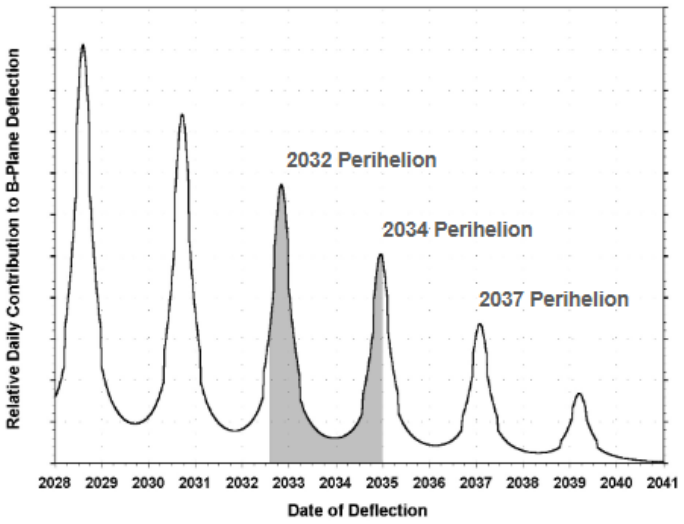



**Figure 6.4: IBD deflection efficiency versus time.**

As noted earlier, we considered a second model of an IBD spacecraft, a repurposed version of the Gateway's PPE. This spacecraft has the basic elements of an IBD mission but would have to be significantly modified. The spacecraft structure would be enlarged for an increased xenon tank capacity of 5000-7000 kg, BHT thrusters would be moved to the other end of the spacecraft, and a station-keeping control system, with appropriate sensors would have to be added. The simulation for this very different IBD spacecraft used two sets of thrusters and propellant usage curves appropriate for the two types of thrusters. Care was taken in the simulation to equalize opposing thrust levels from different types of thrusters with unequal input power levels.

Although this repurposed PPE has more total power available (60 kW) than the purpose-built model described earlier (46 kW), a factor that should make the PPE a more capable spacecraft, the AEPS thrusters have a wider beam divergence than the NEXT-C thrusters, making them less effective for deflection operations. As a result, this spacecraft would have to be stationed closer to the asteroid to get a larger fraction of the ion beam interacting with the asteroid, putting it in a regime where gravity starts to degrade the ion-beam pressure, due to the spacecraft's gravitational acceleration on the asteroid opposing the push of the ion beam on the asteroid. In our simulation for the PPE IBD spacecraft, we chose a compromise on the stationkeeping position at roughly 225 m from the asteroid surface, accounting for larger gravity losses, and assumed only 75% of the ion beam impinges on the surface from the AEPS thrusters.

### *6.4 IBD Mission Options Results*

For each of the two IBD spacecraft models we evaluated the performance of 4 different mission designs and determined the number of IBD spacecraft required to achieve the 3 possible deflection goals: deflecting northward off the Earth, southward off the Earth, and a partial southward deflection to the "safe zone" south of Africa. Tables 6.3, 6.4, and 6.5 show the simulation results for the purpose-built IBD spacecraft for those scenarios. The tables show the number of IBD spacecraft required to reach these goals as a function of asteroid mass, and give the

completion dates for those deflections. A successful northward deflection can be achieved by 1-2 of these IBD spacecraft, while a full southward deflection would require 2-4 such spacecraft. A single IBD spacecraft could achieve the partial southward deflection, provided it was one of the early-launch missions. For the primary and backup IBD missions, a second copy of the spacecraft would be required if the asteroid mass happened to be in the top 10% of the possible mass range.

**Table 6.3: Number of IBD spacecraft & deflection completion dates for northward deflection using the Purpose-Built 46-kW IBD spacecraft.**

| Option: | Ep1 OptA (22kW) | Early1 (46kW) | Early2 (46kW) | Primary (46kW) | Backup (46kW) |
|---|---|---|---|---|---|
| Launch | 10/9/2029 | 4/25/2029 (5.5 mo. earlier) | 6/2/2029 (4.2 mo. earlier) | 10/3/2029 | 4/10/2030 (6.2 mo. later) |
| Arrival | 7/9/2032 | 4/27/2032 | 6/4/2032 | 7/6/2032 | 10/1/2032 |
| Asteroid Mass %ile: | Required Number of Launches: Completion Dates: | | | | |
| Low | 2 Dec 2034 | 1 Mar 2034 | 1 Jun 2034 | 1 Aug 2034 | 1 Dec 2034 |
| 50th | 3 Mar 2035 | 1 Oct 2036 | 1 Nov 2036 | 2 Jun 2034 | 2 Dec 2034 |
| High | 4 Feb 2037 | 2 Feb 2035 | 2 Mar 2035 | 2 Apr 2035 | 2 Dec 2036 |

**Table 6.4: Number of IBD spacecraft & deflection completion dates for southward deflection using the Purpose-Built 46-kW IBD spacecraft.**

| Option: | Ep1 OptA (22kW) | Early1 (46kW) | Early2 (46kW) | Primary (46kW) | Backup (46kW) |
|---|---|---|---|---|---|
| Launch | 10/9/2029 | 4/25/2029 (5.5 mo. earlier) | 6/2/2029 (4.2 mo. earlier) | 10/3/2029 | 4/10/2030 (6.2 mo. later) |
| Arrival | 7/9/2032 | 4/27/2032 | 6/4/2032 | 7/6/2032 | 10/1/2032 |
| Asteroid Mass %ile: | Required Number of Launches: Completion Dates: | | | | |
| Low | 3 Dec 2036 | 1 Feb 2037 | 1 Mar 2037 | 2 Sep 2034 | 2 Jan 2035 |
| 50th | 5 Feb 2037 | 2 Dec 2036 | 2 Jan 2037 | 3 Dec 2034 | 3 Jul 2035 |
| High | 8 Mar 2037 | 3 Mar 2037 | 3 Apr 2037 | 4 Jul 2035 | 4 Jan 2037 |

**Table 6.5: Number of IBD spacecraft & deflection completion dates for partial southward deflection using the Purpose-Built 46-kW IBD spacecraft.**

| Option: | Ep1 OptA (22kW) | Early1 (46kW) | Early2 (46kW) | Primary (46kW) | Backup (46kW) |
|---|---|---|---|---|---|
| Launch | 10/9/2029 | 4/25/2029 (5.5 mo. earlier) | 6/2/2029 (4.2 mo. earlier) | 10/3/2029 | 4/10/2030 (6.2 mo. later) |
| Arrival | 7/9/2032 | 4/27/2032 | 6/4/2032 | 7/6/2032 | 10/1/2032 |
| Asteroid Mass %ile: | Required Number of Launches: Completion Dates: | | | | |
| Low | 1 Nov 2036 | 1 Jan 2033 | 1 Feb 2033 | 1 Mar 2033 | 1 Aug 2034 |
| 50th | 2 Apr 2035 | 1 Nov 2034 | 1 Dec 2034 | 1 Dec 2034 | 1 Jun 2035 |
| High | 3 Dec 2036 | 1 Feb 2037 | 1 Mar 2037 | 2 Sep 2034 | 2 Jan 2035 |

Similarly, Tables 6.6, 6.7, and 6.8 show the corresponding simulation results for the repurposed PPE IBD spacecraft for the same three scenarios (northward, southward, partial southward). Since the number of spacecraft required is larger in some of the cases, this spacecraft is somewhat less capable at achieving required deflections than the purpose-built IBD spacecraft. That is likely due to the wider beam divergence of the AEPS thrusters, as described earlier. Nevertheless, for the partial deflection using the Primary and Backup missions, the PPE IBD performance is almost identical to that of the purpose-built IB spacecraft in terms of the number of spacecraft.

**Table 6.6: Number of IBD spacecraft & deflection completion dates for northward deflection using the Repurposed PPE 60 kW IBD spacecraft.**

| Option: | Early1 | Early2 | Primary | Backup |
|---|---|---|---|---|
| Launch | 4/14/2029 (5.4 mo. earlier) | 6/2/2029 (4 mo. earlier) | 10/2/2029 | 4/3/2030 (6.2 mo. later) |
| Arrival | 3/16/2032 | 5/4/2032 | 7/26/2032 | 10/31/2032 |
| Asteroid Mass %ile: | Required Number of Launches: Completion Dates: | | | |
| Low | 1 Jan 2033 | 1 Jan 2033 | 1 May 2033 | 1 Nov 2034 |
| 50th | 1 Jan 2035 | 2 Jan 2033 | 2 Apr 2033 | 2 Oct 2034 |
| High | 2 Jul 2034 | 2 Oct 2034 | 3 Jun 2033 | 3 Nov 2034 |

**Table 6.7: Number of IBD spacecraft & deflection completion dates for southward deflection using the Repurposed PPE 60 kW IBD spacecraft.**

| Option: | Early1 | Early2 | Primary | Backup |
|---|---|---|---|---|
| Launch | 4/14/2029 (5.4 mo. earlier) | 6/2/2029 (4 mo. earlier) | 10/2/2029 | 4/3/2030 (6.2 mo. later) |
| Arrival | 3/16/2032 | 5/4/2032 | 7/26/2032 | 10/31/2032 |
| Asteroid Mass %ile: | Required Number of Launches: Completion Dates: | | | |
| Low | 2 Jan 2033 | 2 Feb 2033 | 2 Jul 2033 | 2 Nov 2034 |
| 50th | 2 Mar 2035 | 3 Oct 2033 | 3 Dec 2034 | 3 Feb 2035 |
| High | 4 Aug 2034 | 4 Nov 2034 | 5 Nov 2034 | 5 Jan 2035 |

**Table 6.8: Number of IBD spacecraft & deflection completion dates for partial southward deflection using the Repurposed PPE 60 kW IBD spacecraft.**

| Option: | Early1 | Early2 | Primary | Backup |
|---|---|---|---|---|
| Launch | 4/14/2029 (5.4 mo. earlier) | 6/2/2029 (4 mo. earlier) | 10/2/2029 | 4/3/2030 (6.2 mo. later) |
| Arrival | 3/16/2032 | 5/4/2032 | 7/26/2032 | 10/31/2032 |
| Asteroid Mass %ile: | Required Number of Launches: Completion Dates: | | | |
| Low | 1 Nov 2032 | 1 Nov 2032 | 1 Dec 2032 | 1 May 2034 |
| 50th | 1 Jun 2033 | 1 Sep 2033 | 1 Dec 2034 | 1 Jan 2035 |
| High | 2 Jan 2033 | 2 Feb 2033 | 2 Jul 2033 | 2 Nov 2034 |

## 7. Nuclear Explosive Device (NED) Mission Campaign Analysis

For missions employing Nuclear Explosive Devices (NEDs) to deflect the asteroid, we assume that the NED carrier spacecraft rendezvouses with the asteroid, rather than attempting to detonate the NEDs in proximity to the asteroid during a high-speed intercept. In this section, we detail the NED modeling, the NED deflection mission design strategy, and the asteroid deflection performance.

### *7.1 NED Mission Campaign Strategy*

The concept of operations for the NED deflection missions involves an NED carrier spacecraft employing SEP and carrying multiple deployable free-flyer NED subspacecraft. The NED carrier rendezvouses with the asteroid and then spends up to 4 months characterizing the asteroid, which includes measuring the asteroid's mass. Knowledge of the asteroid's mass, shape, and other properties allows the Height of Burst (HOB) to be selected relatively precisely for the standoff NED detonations near the asteroid. Standoff NED detonations near an asteroid produce radiation that ablates a thin layer of asteroid surface material, which then blows off from the asteroid. That causes the asteroid to recoil in the opposite direction, thereby imparting ΔV to the asteroid. As with KIs, this ΔV is impulsive, i.e., effectively instantaneous.

Based on the asteroid properties knowledge at Epoch 2, the yield of each NED is selected to be 100 kt. The total mass of a basic subspacecraft carrying such an NED, which includes the necessary subsystems (e.g., thrusters, camera, short-range communications, etc.), is assumed to be approximately 250 kg.

After characterizing the asteroid and planning appropriate HOBs for the NED detonations, the NED carrier spacecraft begins deflection operations two months prior to the asteroid's next perihelion. Deflection operations are assumed to span up to 4 months, if necessary, centered on the asteroid's perihelion, and with a minimum of 14 days between detonations, allowing time to measure the effect on the asteroid before the next detonation. This provides significant operational flexibility. During an NED detonation, the NED free-flyer subspacecraft is deployed and commanded to move to the correct coordinates above the asteroid's surface. The NED carrier spacecraft moves to the opposite side of the asteroid before detonation, for protection. The NED is then commanded to detonate and the results are assessed. Multiple detonations may be performed if necessary, and they each follow the same procedure outlined above.

*7.2 Spacecraft Trajectory Analysis*

As with rendezvous trajectories for reconnaissance and IBD, SEP is enabling for delivering the necessary payload mass for NED deflection. To map the optimal solution space given the coupling between trajectory performance and SEP parameters, a many-objective stochastic optimizer is applied while trading the parameters outlined in Table 7.1. Launch dates between October 2029 (five years after ATP) to December 2036 are considered in the optimization. The five objective functions listed in Table 7.1 are optimized simultaneously to generate Pareto-optimal solutions. All solutions launch on a Falcon Heavy Expendable launch vehicle and the optimizer considers different flyby sequences with up to three flybys considered with any combination of Earth, Venus, or Mars.

**Table 7.1. NED Rendezvous Trajectory Optimization Variables (left) and Objective Functions (right).**

| Trade Parameters | Values |
|---|---|
| **Launch date** | October 2029 (ATP+5 years) to December 2036 |
| **Time of flight** | Up to 4 years |
| **EOL power** | 10 to 46 kW |
| **EP thruster type** | XR5, XIPS-25, NEXT-C, AEPS/HERMeS |
| **Number of thrusters** | 2 to 6 |

| Objectives |
|---|
| Maximize delivered mass |
| Minimize time of flight |
| Minimize launch date |
| Minimize EOL power |
| Minimize number of thrusters |

Estimated payload mass versus arrival date for the optimal trajectories is plotted in Figure 7.1 with the color indicating the end-of-life solar array power. Solutions with 10- to 22-kW SEP systems are well-represented in the optimal solution space. with many options delivering more than the estimated 2,400 kg requirement for the NED payload for a variety of launch and arrival dates. SEP power levels between 10 and 22 kW are in-family with past and current interplanetary SEP spacecraft power levels such as Dawn and Psyche.

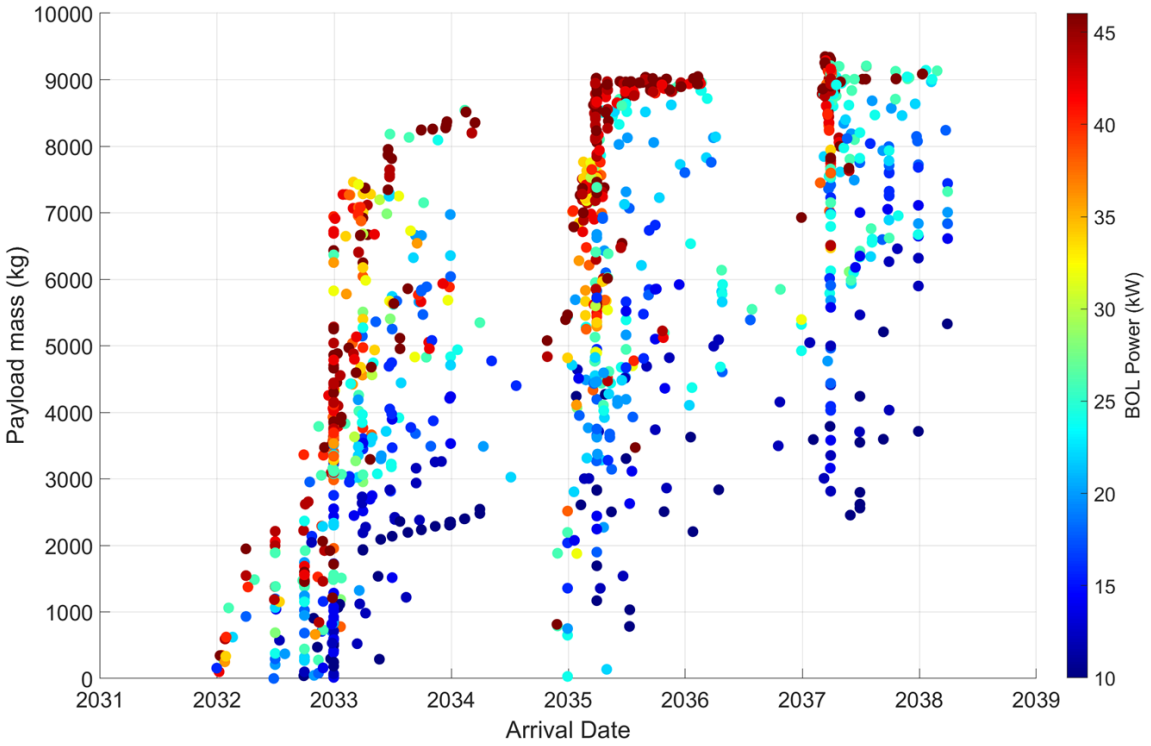



**Figure 7.1. Pareto-optimal solution space for NED deflection rendezvous trajectories.**

Primary, backup, and “last-ditch” options are selected from the optimal solutions and listed in Table 7.2. The primary solution launches in April 2031, approximately 6.5 years after ATP, and requires a 16-kW SEP system to deliver roughly 4,680 kg to the asteroid in January 2033. A backup solution launches two years later in April 2033 and only requires a 12-kW SEP system to deliver over 5,000 kg. The last-ditch option launches in June 2035 and arrives in September 2038, six months ahead of the final perihelion before impact. An early launch option was also considered for a scenario in which a dedicated precursor rendezvous reconnaissance mission was not launched and the SEP spacecraft carrying the NED payload would also be conducting initial rendezvous reconnaissance. The early option launches in June 2029, 4.7 years after ATP, and arrives in December 2031. Trajectory plots for each of the NED rendezvous options are illustrated in Figures 7.2 and 7.3.

**Table 7.2. Exemplar Pareto-optimal SEP rendezvous mission options for NED deflection.**

| Case | Launch Date | Arrival Date | Time of Flight [years] | Launch Vehicle | SEP EOL Power at 1AU | Flyby sequence | Delivered Mass to Asteroid [kg] | Estimated Payload Mass (kg) |
|---|---|---|---|---|---|---|---|---|
| Early | 2029-06-30 | 2031-12-30 | 2.50 | FHE | 26 | Direct | 4878 | 3012 |
| Primary | 2031-04-14 | 2033-01-12 | 1.75 | FHE | 16 | Direct | 4684 | 2928 |
| Backup | 2033-04-16 | 2035-10-15 | 2.50 | FHE | 12 | Direct | 5078 | 3360 |
| Last-Ditch | 2035-06-26 | 2038-09-01 | 3.18 | FHE | 22 | Direct | 4222 | 2400 |

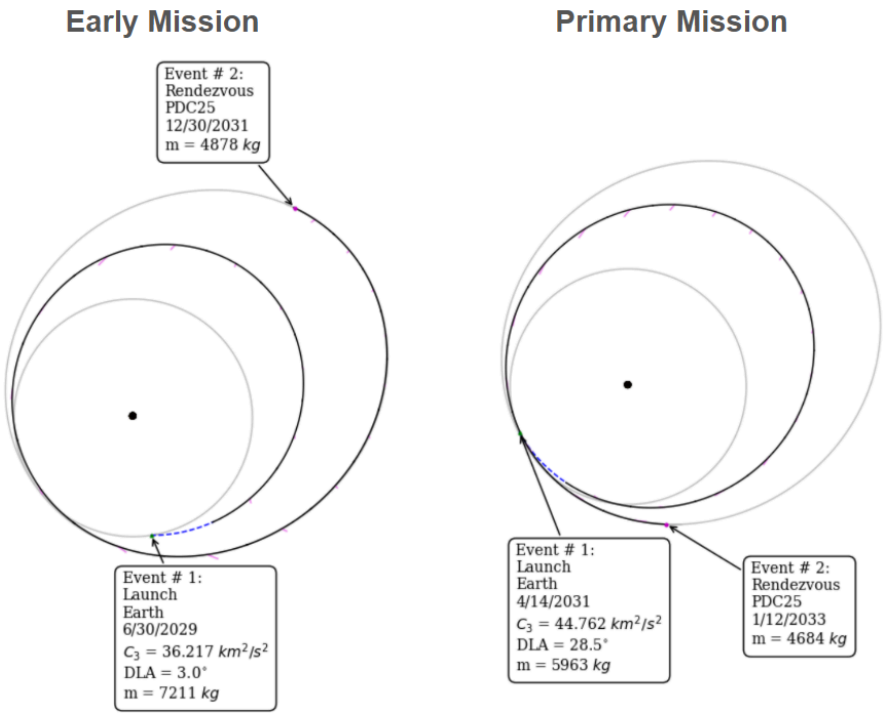



**Figure 7.2. Trajectory plots for early (left) and primary (right) NED deflection rendezvous options.**

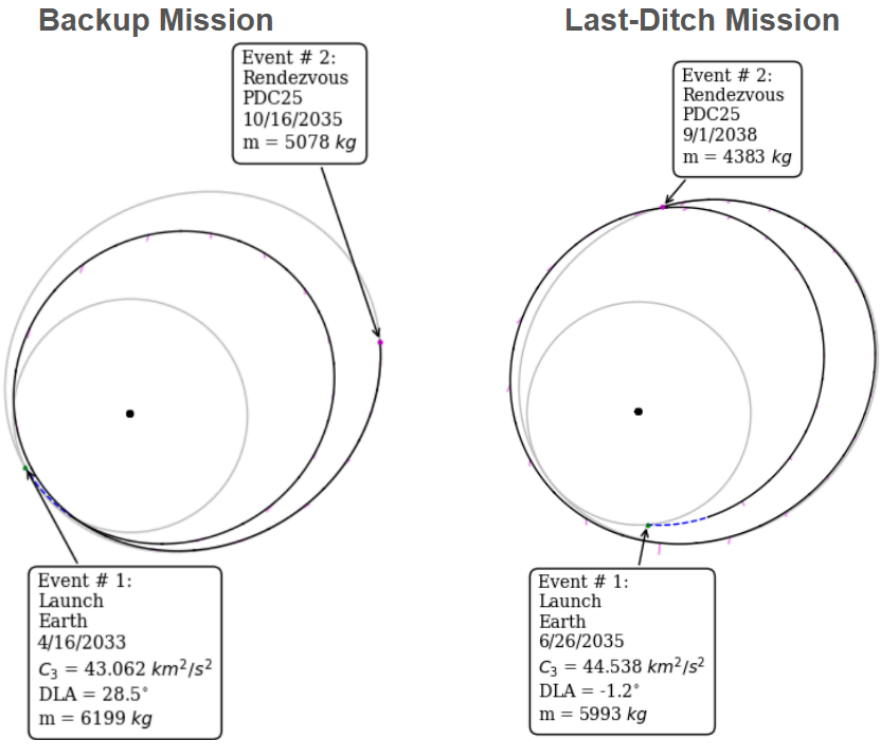



**Figure 7.3. Trajectory plots for backup (left) and last-ditch (right) NED deflection rendezvous options.**

*7.3 Standoff Nuclear Detonation Modeling*

*7.3.1 ARES modeling methods*

We used the multi-physics, mesh-based hydrodynamic simulation code named ARES[5] developed at LLNL [44,45] to simulate standoff nuclear detonation scenarios. In these simulations the asteroid is modeled as a homogeneous sphere in a 2D axisymmetric coordinate system. The ARES simulations were initialized using the energy deposition model from Burkey et al. [12,13], which approximates the X-rays absorbed by the asteroid's surface following the illumination from a nuclear explosive device (NED). The Burkey et al. model, based on extensive radiation-hydrodynamic simulations, assumes a constant 1-2 keV X-ray blackbody spectrum and is robust across various input parameters, including illumination times (10 – 100 ns), fluences ($10^{-4} - 1\ kt\ m^{-2}$), microporosities ($\phi = 0 - 0.8$), and asteroid compositions (silicon dioxide, $SiO_2$, forsterite, $MgSiO_4$, ice, and iron). To account for porosity effects, the ARES porosity model dynamically reduces porosity when the pressure exceeds a reference crush curve pressure, ranging from 1.1-4.8 MBar for our simulations. We modeled each hypothetical asteroid with a forsterite equation of state (reference density $\rho_0 = 3.22\ g\ cm^{-3}$) adapted from M-ANEOS [35], and ran simulations using blackbody spectrum temperatures of 1 and 2 keV. Finally, we ran these simulations without incorporating material strength models in ARES. Although modeling material damage may provide additional insight, we deflect these asteroids at relatively small

[5] ARES is the name of the code, and it is not an acronym.

velocities which reduces the impact that strength/damage models have on the overall material dynamics.

Burkey et al. quantified the total uncertainty from the deposition model to be 15.8% by summing contributions from error sources such as meshing, material models, and time-dependent illumination variability. It is important to note that realistic asteroid properties, including irregular shapes, heterogeneous compositions, and complex internal structures, introduce far greater uncertainty to a final deflection velocity (ΔV) estimate. By employing the Burkey et al. model, we substantially reduce the computational resources required to complete a full 2D radiation transport simulation from start to finish. With the momentum carried away by the "blown off" material from the NED's X-ray exposure ("blowoff momentum", $\vec{p}_b\,\vec{p}_b$) used as the primary metric for comparison, Burkey et al. showed consistent results within ~10% between simulations with and without radiation transport, validating the reliability of this approach.

*7.3.2 Cassio modeling methods*

We also conducted nuclear stand-off burst models using simplified X-ray energy pill sources in the Eulerian radiation hydrocode Cassio [47]. Cassio uses the Radiation Adaptive Grid Eulerian (RAGE) [48] hydrodynamics package, and adds an implicit Monte Carlo (IMC) radiation transport algorithm [50] for X-ray light transport. Verification and validation of Cassio against shocks in porous silicates was reported in [49]. We used the Sesame EOS database [39], aluminum EOS 3720 and opacity tables for the simplified NED energy pill and the basalt EOS 7530 [46] and granite opacity tables for the target asteroid.

*7.4 NED Detonation Modeling Results*

To meet the Epoch 1 mission requirement of a 4 cm/s deflection velocity, we ran dozens of two-dimensional (2D) hydrodynamic simulations using ARES with a 1,000 kt NED initialized with the Burkey et al. model to determine heights-of-burst (HOBs) for achieving the target ΔV. In total, we obtained two HOBs for each blackbody spectrum temperature to bracket the mission ΔV requirement to within $\lesssim 15 \lesssim 15$ percent. We show an example of the results for the 50$^{th}$ Percentile asteroid (D = 127 m) in Figure 7.4, which shows the deflection velocity curves in the left panel, and visualizes the simulated asteroid and the ablated material in the right panel (color-coded by kinetic energy per unit volume). We deflected the asteroids to within $\lesssim 15$ percent of ΔV = 4 cm/s with HOBs ranging from 950-1700 m for the 5$^{th}$ percentile asteroid, 575-1,100 m for the 50$^{th}$ Percentile, 300-750 m for the 95$^{th}$, and 110-450 m for the largest (where the lower and upper bounds correspond to a 1 and 2 keV source, respectively).

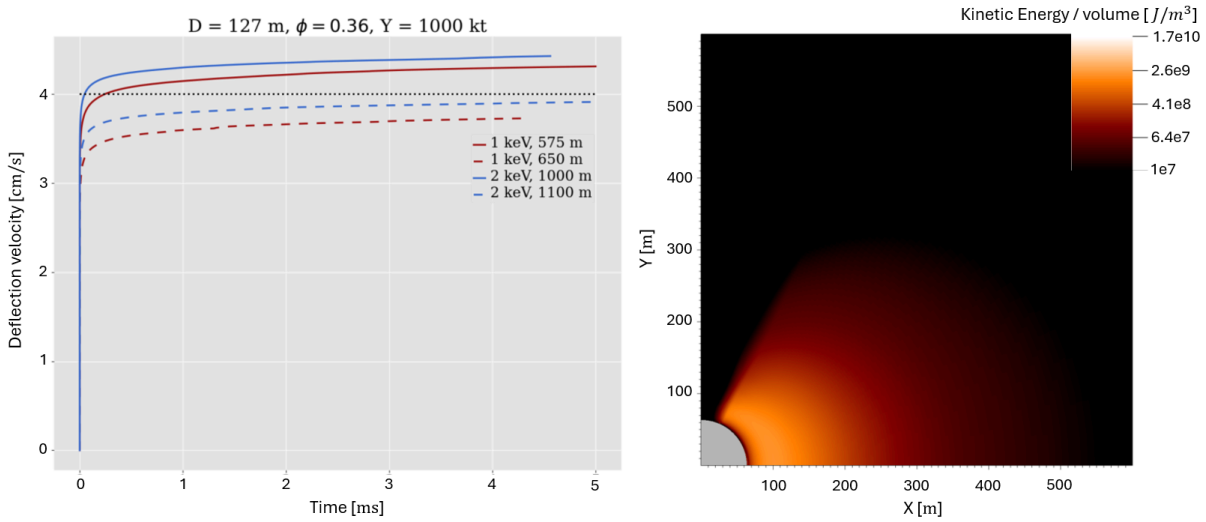



**Figure 7.4. Deflection velocity curves for the Epoch 1 - 50th Percentile asteroid (D = 127 m) are shown in the left panel, illustrating results for both X-ray blackbody spectrum temperatures at two HOBs each. The right panel presents an image from one of the 2D ARES simulations, where ablated material is color-coded by the kinetic energy per volume (right panel).**

Thanks to the post-Epoch 1 flyby reconnaissance mission, the asteroid's physical properties were more accurately constrained for Epoch 2. These constraints provided a relatively narrow range of properties, enabling us to focus on modeling three representative cases: the minimum, median, and maximum mass asteroids corresponding to $M = 2 \times 10^9\ kg, 3.93 \times 10^9\ kg$ and $7.03 \times 10^9\ kg$, respectively. For Epoch 2, we adopted a smaller NED yield of 100 kt, compared to the 1,000 kt yield used in Epoch 1. This choice offers operational flexibility, allowing multiple NEDs to fit onto the spacecraft. This flexibility is crucial if multiple impulses are necessary to achieve deflection without risking accidental disruption of the asteroid. Using the ARES simulation framework mentioned above, we modeled the deflection of these three asteroid realizations by both 4% and 10% of their escape velocities. Currently, there is no detailed discussion in the literature regarding the associated uncertainty related to the deflection velocity from the nuclear mitigation framework. Thus, we conservatively assumed an uncertainty factor of 2.5 in ΔV for the 4% escape velocity simulations. This approach accounts for potential overperformance of the deflection velocity, ensuring that even if the actual ΔV exceeds the target by a factor of 2.5, the asteroid will still be deflected to within 10% of its escape velocity. This operational strategy minimizes the risk of accidental disruption while maintaining deflection effectiveness.

The reconnaissance mission data also constrained the asteroid's dimensions to a roughly 1:1:2 axis ratio. However, due to the lack of capability in ARES to model non-spherical asteroid shapes, we approximated the asteroid using the spherical equivalent radius and corresponding density to match the masses for the three realizations in each 2D simulation. For the maximum mass asteroid, the reported density exceeded the reference density of Forsterite. To address this, we maintained the porosity value and scaled up the asteroid's size until the maximum mass was achieved. The final model for this asteroid had a diameter of $D = 163\ m$, and

density of $\rho = 3.09\ g\ cm^{-3}$. Simulation results for deflections at 4% and 10% escape velocity are presented in Figures 7.5 and 7.6, respectively. These figures show that the range of the HOBs is between 450 – 1950 meters for ΔV =4% $V_{escape}$ and 240 – 1300 meters for ΔV =10% $V_{escape}$. We highlight the fact that all HOBs reported in these analyses are achievable with current asteroid proximity operations capabilities, and none of them would drive the proximity operations propellant budget.

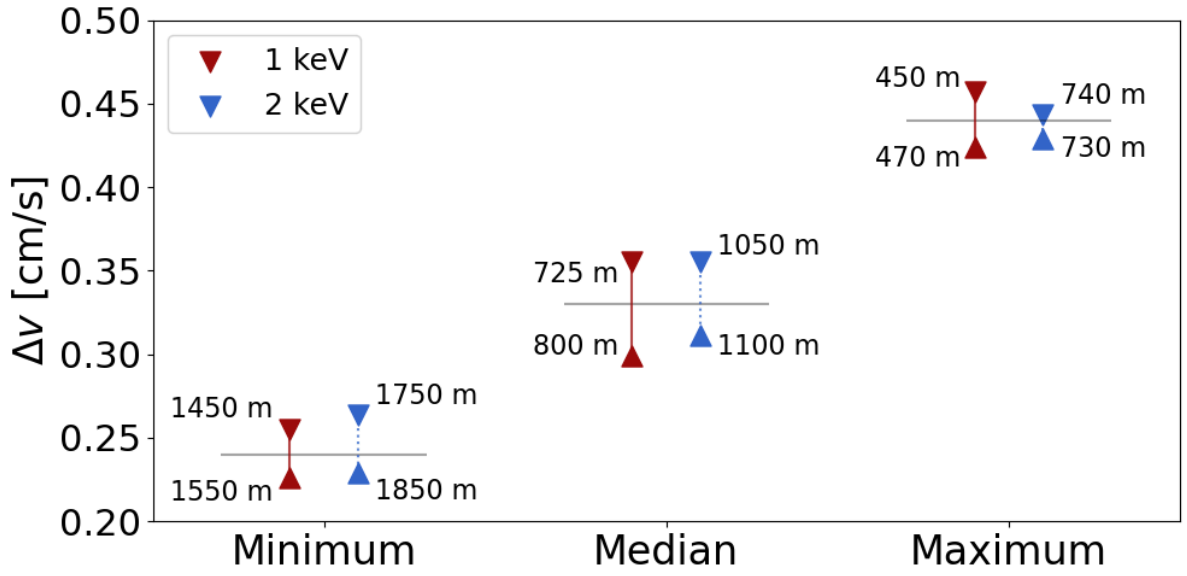



**Figure 7.5. Similar to Figure 7.6, results from the Epoch 2 NED simulation suite, illustrating the HOBs required to achieve a deflection of approximately 4 percent of the escape velocities for asteroids with minimum (D = 147 m), median (D = 150 m), and maximum mass (D = 163 m) within the simulated population.**

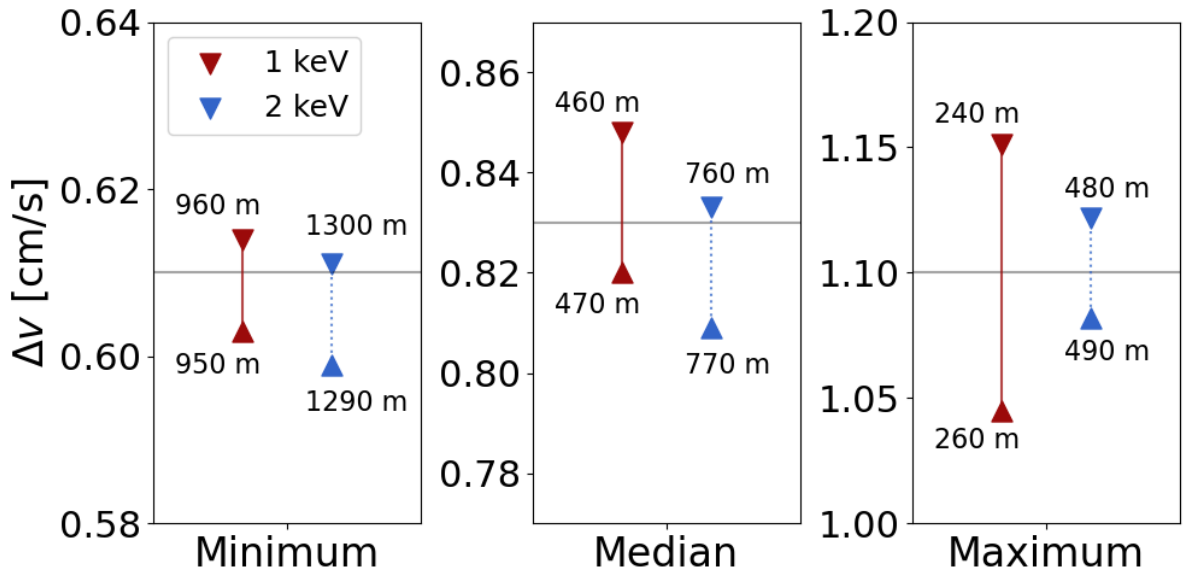



**Figure 7.6. Similar to Figure 7.5, only showing the HOBs needed to deflect the three asteroid realizations by 10 percent of their respective escape velocities.**

We ran additional simulations of a 100 kt stand-off burst at a HOB of 1,150 m above the 95th percentile hypothetical threat object case using the Cassio radiation hydrocode described above. These simulations, conducted using different numerical methods, yielded broadly similar results to those conducted in ARES. The calculations predict a ΔV ≥ 0.2 cm/s by t = 0.00015 s, resulting from the explosive decompression of 7.3 x $10^5$ kg of ablated target material. The similarity of results between different approaches lends support to our ΔV predictions.

*7.5 NED Mission Options Results*

The amount of ΔV required to deflect the asteroid off the Earth in the northward or southward directions, or to perform a partial southward deflection of the asteroid, is shown in Table 7.3 for each of the 4 asteroid perihelions remaining before the 2041 Earth impact epoch. Specifically, Table 7.3 shows the amount of ΔV required for deflection at the edges of a 4-month interval centered on each perihelion. Table 7.4 shows the ΔV magnitudes equal to 4% $V_{escape}$ and 10% $V_{escape}$ for the Low Mass, 50th Percentile Mass, and High Mass realizations of the asteroid.

**Table 7.3: ΔV requirements for asteroid deflection (full northward or southward, and partial southward) at the edges of a 4-month interval centered on the asteroid perihelia remaining before Earth impact.**

| Perihelion | Northward DV (cm/s) +/-2 months | Southward DV (cm/s) +/-2 months | Partial Southward DV (cm/s) +/-2 months |
|---|---|---|---|
| 11/1/2032 | 0.67 | 1.39 | 0.45 |
| 12/15/2034 | 0.89 | 1.86 | 0.60 |
| 1/28/2037 | 1.34 | 2.78 | 0.90 |
| 3/14/2039 | 2.67 | 5.55 | 1.80 |

**Table 7.4: ΔV magnitudes equal to 4% $V_{escape}$ and 10% $V_{escape}$ for the Low Mass, 50th Percentile Mass, and High Mass realizations of the asteroid.**

| | 4% Vesc (cm/s) | 10% Vesc (cm/s) |
|---|---|---|
| **Low Mass** | 0.24 | 0.60 |
| **50th %tile Mass** | 0.33 | 0.83 |
| **High Mass** | 0.42 | 1.06 |

Dividing the ΔV magnitudes into the deflection ΔV requirements in Table 7.3 yields the number of NED detonations required to carry out the deflection, as a function of: whether the detonations target 4% $V_{escape}$ or 10% $V_{escape}$, at which asteroid perihelion the deflection is being performed, and whether the deflection is full northward (N), full southward (S, or partial southward (P). The resulting required numbers of NED detonations with each ΔV ≤ 4% $V_{escape}$ are shown in Table 7.5, and the results with each ΔV ≤ 10% $V_{escape}$ are shown in Table 7.6

**Table 7.5: Number of NED detonations required for full northward (N), full southward (S), or partial southward (P) asteroid deflection, for each NED mission launch opportunity and associated asteroid perihelion at which deflection would be performed, assuming each ΔV ≤ 4% $V_{escape}$. The number of NEDs that can be delivered by the NED carrier are shown at the bottom of the table, and cases that would require more NEDs than can be delivered by a single NED carrier are marked in red.**

| | # Impulses for Deflection w/ Each <= 4% Vesc | | | | | | | | | | | |
|---|---|---|---|---|---|---|---|---|---|---|---|---|
| | 2032 Deflection (Early) | | | 2034 Deflection (Primary) | | | 2037 Deflection (Backup) | | | 2039 Deflection (Last-Ditch) | | |
| **Asteroid Mass** | **N** | **S** | **P** | **N** | **S** | **P** | **N** | **S** | **P** | **N** | **S** | **P** |
| **Low Mass** | 3 | 6 | 2 | 4 | 8 | 2 | 6 | 12 | 4 | 11 | 23 | 7 |
| **50th %tile Mass** | 2 | 4 | 1 | 3 | 6 | 2 | 4 | 8 | 3 | 8 | 17 | 5 |
| **High Mass** | 2 | 3 | 1 | 2 | 4 | 1 | 3 | 7 | 2 | 6 | 13 | 4 |
| | 12 NEDs Available | | | 11 NEDs Available | | | 13 NEDs Available | | | 9 NEDs Available | | |

**Table 7.6: Number of NED detonations required for full northward (N), full southward (S), or partial southward (P) asteroid deflection, for each NED mission launch opportunity and associated asteroid perihelion at which deflection would be performed, assuming each ΔV ≤ 10% $V_{escape}$. The number of NEDs that can be delivered by the NED carrier are shown at the bottom of the table.**

| | # Impulses for Deflection w/ Each <= 10% Vesc | | | | | | | | | | | |
|---|---|---|---|---|---|---|---|---|---|---|---|---|
| | 2032 Deflection (Early) | | | 2034 Deflection (Primary) | | | 2037 Deflection (Backup) | | | 2039 Deflection (Last-Ditch) | | |
| **Asteroid Mass** | **N** | **S** | **P** | **N** | **S** | **P** | **N** | **S** | **P** | **N** | **S** | **P** |
| **Low Mass** | 1 | 2 | 1 | 1 | 3 | 1 | 2 | 5 | 1 | 4 | 9 | 3 |
| **50th %tile Mass** | 1 | 2 | 1 | 1 | 2 | 1 | 2 | 3 | 1 | 3 | 7 | 2 |
| **High Mass** | 1 | 1 | 1 | 1 | 2 | 1 | 1 | 3 | 1 | 3 | 5 | 2 |
| | 12 NEDs Available | | | 11 NEDs Available | | | 13 NEDs Available | | | 9 NEDs Available | | |

Tables 7.5 and 7.6 show that more than enough NEDs can be delivered to the asteroid by a single NED carrier spacecraft for nearly all combinations of mission launch opportunity and deflection direction, except for full southward deflection at the final asteroid perihelion before Earth impact, or full northward deflection at that perihelion for the Low Mass asteroid, with ΔV ≤ 4% $V_{escape}$. If ΔV ≤ 10% $V_{escape}$ then all cases are viable. Overall, with either ΔV threshold, a single NED carrier spacecraft is capable of deflecting the asteroid for any of the four launch opportunities. This performance is summarized in Table 7.7.

**Table 7.7: Number of NED carrier spacecraft required to deflect the asteroid, and the associated deflection completion date, for the Early, Primary, Backup, and Last-Ditch NED deflection mission launch opportunities.**

| Number of NED Spacecraft Required to Complete Deflection & Completion Date | | | | |
|---|---|---|---|---|
| | Launch Opportunity (Launch Year) | | | |
| **Asteroid Mass** | **Early (2029)** | **Primary (2031)** | **Backup (2033)** | **Last-Ditch (2035)** |
| **Low Mass** | 1<br>Sep 2032 | 1<br>Dec 2034 | 1<br>Mar 2037 | 1<br>May 2039 |
| **50th %tile** | 1<br>Sep 2032 | 1<br>Dec 2034 | 1<br>Jan 2037 | 1<br>Mar 2039 |
| **High Mass** | 1<br>Sep 2032 | 1<br>Oct 2034 | 1<br>Jan 2037 | 1<br>Mar 2039 |

## 8. Discussion

With the foregoing analyses of mission requirements and performance for each candidate deflection mission type in hand, we can generate recommendations for decision makers to consider regarding how to proceed, and identify the branches in

the associated decision tree. In this section, we formulate recommendations about mission options, including key assumptions, and compare and contrast the candidate deflection methods in the context of the recommendations and decision tree.

### *8.1 Key Assumptions for Making Recommendations about Mission Options*

In order to generate recommendations for decision makers to consider regarding mission options, it is necessary to specify the underlying assumptions. These assumptions about what was done, or not done, between October 2024 (Epoch 1) and April 2028 (Epoch 2) determine what can be credibly done between April 2028 and the mission launch dates.

We assume that Phase A/B work was performed for the SEP RRS mission from October 2024 to October 2026, and the work continued after Earth impact probability reached 100% in late 2025. This is necessary in order for the RRS mission to be ready for launch in December 2029. That is important because the RRS mission would be necessary for a KI campaign should decision makers elect to deploy KIs, but the decision to complete the RRS development cannot wait until the deployment decision is made. Similarly, we also assume that Phase A/B work for each deflection mission type (i.e., KI, IBD, NED) was performed from October 2024 to October 2026. However, downselection between the deflection mission types must wait until the flyby reconnaissance data are processed in April 2028.

Another assumption critical for IBD is that investments were made to provide the necessary hardware for the IBD spacecraft (NEXT-C thrusters/PPUs and/or a reconfigured Gateway PPE spacecraft) to the extent necessary to make the needed number of IBD spacecraft ready for launch between April 2029 and April 2030 (only 1–2 years after the flyby reconnaissance mission reaches the asteroid). Note that there is currently no active production line for the NEXT-C gridded-ion thrusters and PPUs. Therefore, successfully building multiple sets of 6 thrusters and 6 PPUs in time for a 2029–2030 launch could be very challenging, even if the necessary investments are made. Additionally, we note that PPE is currently scheduled for launch in 2028 and repurposing it would offer challenges, and could necessitate investing in building 1–2 copies of PPE, with a modified configuration.

Finally, we assume that any campaign options requiring multiple spacecraft would be logically distributed among those nations that would be participating in their development, launch, and operations.

### *8.2 Mission Options Recommendations*

After considering the mission performance presented previously for each deflection mission type, the underlying assumptions, and various other factors including logistics and effects on impact damage risk, we make the following three recommendations as to how decision makers might proceed:

1. Decide whether the deflection will be northward or southward.

   Note that choosing northward would eliminate KI from consideration, leaving only IBD and NED as options. Additionally, the deflection distance required for

total deflection southwards is roughly twice the northward deflection distance. Therefore, the mission requirements vary significantly (by a factor of ~2) for IBD according to whether the deflection is northward or southward. Conversely, the mission requirements for NED do not depend on whether the deflection is northward or southward. Finally, there are roughly 6 times more people living along the northward corridor (~85% of corridor population; ~80–120 million people) than along the southward corridor (~15% of corridor population; ~15-25 million people). Therefore, significantly more people are placed at risk during northward deflection operations than during southward deflection operations.

2. If the southward deflection is selected, then finish assessing whether a partial deflection option is considered safe/acceptable, and then decide whether partial deflection or total deflection will be the mission goal.

   Note that the mission requirements vary significantly for KI and IBD according to whether partial or total deflection is pursued. Additionally, KI is not precise enough to target the partial deflection zone with confidence on its own, but IBD can (potentially in combination with a KI). Meanwhile, the mission requirements for NED do not depend on whether partial or total deflection is pursued. Finally, even if the total southward deflection is selected as the mission goal, partial deflection may still be an acceptable backup/contingency option.

3. Select a deflection mission type (KI, IBD, or NED), complete its development, and deploy it. Multiple factors must be considered, including technical maturity, cost, and geopolitical considerations.

   Table 8.1 compares the overall mission requirements for each of the three deflection mission types.

**Table 8.1. Comparison of the three deflection mission types according to required number of spacecraft / launches and total spacecraft mass launched.**

| Deflection Mission Type | Northward Total Deflection | | Southward Total Deflection | | Southward Partial Deflection | |
|---|---|---|---|---|---|---|
| | Number of Spacecraft / Launches | Total Spacecraft Mass (kg) | Number of Spacecraft / Launches | Total Spacecraft Mass (kg) | Number of Spacecraft / Launches | Total Spacecraft Mass (kg) |
| **KI + RRS** | N/A | N/A | 5--8 | 5,400-8,300 | 3 | 4,500 |
| **IBD** | 2--3 | 17,000-38,400 | 4--5 | 40,000-50,000 | 2 | 17,000-25,600 |
| **NED** | 1 | 6,000-7,200 | 1 | 6,000-7,200 | 1 | 6,000-7,200 |

From the results in Table 8.1, we make the following observations:

KI requires more spacecraft than NED does (5-8 vs. 1) due to the need to avoid accidental asteroid fragmentation, and to handle uncertainties in asteroid mass and β. Unlike NED and IBD, KI cannot deflect northward, only southward. However, KI

isn't precise enough to confidently carry out a southward partial deflection on its own. Note that the KI missions require the support of the RRS mission currently under development for launch in December 2029 (and arriving at the asteroid in December 2031, prior to when the first KI spacecraft would strike the asteroid).

IBD requires significantly more total spacecraft mass than NED or KI (and significantly more mass than previous interplanetary missions). The number of IBD spacecraft required for a southward total deflection is comparable to KI (e.g., 4-5 vs. 5-8).

Deploying a combination of KI and IBD may also be considered, to provide some redundancy. The separate RRS would not necessarily be needed in that case because the IBD spacecraft could perform the RRS functions. A KI + IBD partial deflection mission campaign would require 1-3 KIs and 1 IBD spacecraft. IBD could provide orbital "clean-up" capability for targeting the partial deflection zone precisely. Meanwhile, a KI + IBD total deflection mission campaign could involve various combinations of KI and IBD spacecraft, bound by the numbers in the table above.

Finally, 1 NED-carrier spacecraft, carrying 9-12 free-flyer NEDs (assuming 100 kt each), can achieve total deflection northward or southward, or partial deflection southward. The total spacecraft mass is in family with interplanetary mission flight heritage.

Figure 8.1 summarizes the decision tree available to decision makers, based on the recommendations described above.

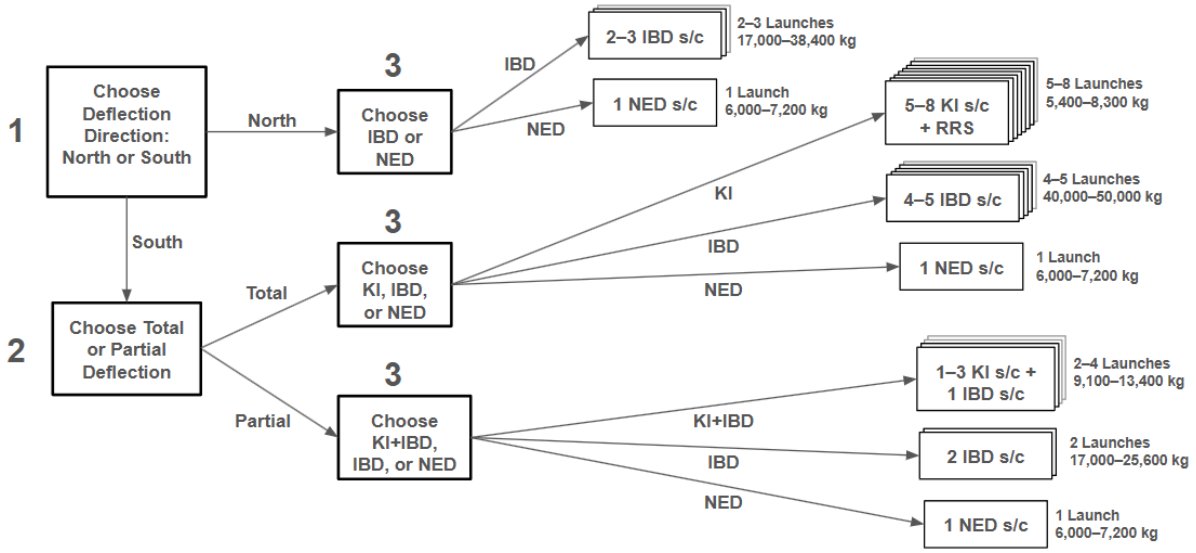



**Figure 8.1. Space mission options selection decision tree.**

*8.3 Additional Considerations*

KIs offer the second-most launch opportunities, the third-earliest deflection completion dates, and the second-latest launch and deflection opportunities. KI missions launch between 2030 and 2035, and complete the deflection 2034-2037.

IBD offers the fewest launch opportunities, the second-earliest deflection completion dates, and does not have any later launch opportunities. IBD must operate at the soonest perihelion (2032) in order to be effective. IBD missions must launch between 2029 and 2030, and complete the deflection between 2033-2037.

NED deflection offers the most launch opportunities, the earliest deflection completion dates, and the latest launch and deflection opportunities. NED missions have 4 distinct launch opportunities in 2029, 2031, 2033, and 2035, and complete the deflection between 2032-2039 (depending on launch date). We note that one or more NED missions could be prepared for launch as a backup option even if decision makers select KI or IBD as the primary deflection approach.

Comparison of total available time for spacecraft design and construction (assuming ATP in October 2024):

- There are 5.75 years before the first KI launch, plus additional ~2-3 years to build KIs 2 through 7.
- There are about 5 years available to build the RRS (in parallel with the KI spacecraft construction).
- There are 4.5-5.5 years available to build the IBD spacecraft before launch. Again, note that NEXT-C thruster/PPU production may be challenging.
- There are 4.7, 6.5, 8.5, or 10.5 years available to build the NED carrier before launch, depending on which launch opportunity is utilized.

Also, note that for any of the deflection mission types, some number of additional spacecraft beyond the numbers stated herein would also need to be launched to provide margin against failures, including the RRS.

Finally, we note that there will be legal/policy issues pertaining to any deflection system, not only for NEDs. Additionally, each type of spacecraft (KI, IBD, NED carrier) involves various novel design elements that introduce various risks because no type of deflection spacecraft is fully tested and operational.

*8.4 Strengths and Weaknesses of KI, IBD, and NED*

In addition to the foregoing analyses of mission requirements and available performance, the various strengths and weaknesses of each deflection mission type should also be considered when making selections. Here, we list notable strengths and weaknesses for KI, IBD, and NED.

KI Strengths:

- KI is the only asteroid deflection technique that has been demonstrated in space on an asteroid (DART). Furthermore, the size of the target asteroid in this scenario (~150 m) is similar to the size of DART's target asteroid, Dimorphos.
- KI is not affected by nuclear-related legal/policy issues, although legal/policy issues likely exist for any deflection system (even if those issues haven't been appreciated yet).

- KIs are relatively simple designs with few “moving parts” and don’t need to perform complex operations over long periods of time. This improves mission reliability and probability of success, all else being equal.

KI Weaknesses:

- The KI missions called for here approach the asteroid at speeds roughly twice as fast as DART, and some of the KI spacecraft masses called for are several times larger than DART.
- Asteroid response (e.g., momentum enhancement factor, β) is difficult to predict and may vary across multiple impacts. This drives spacecraft mission campaign design (more, smaller KIs and/or the need to tune each KI spacecraft mass individually before launch or in flight).
- As an impulsive technique, there is some risk of asteroid fragmentation (particularly for this asteroid, which may be a contact binary). Steps taken to avoid fragmentation result in a more complex design involving multiple KIs instead of one.
- 4–7 KI spacecraft/launches are required for deflecting the asteroid, to avoid fragmentation risk, plus a separate RRS mission.
- While DART has demonstrated a single kinetic impact on an asteroid, multiple kinetic impacts on an asteroid have not been demonstrated. Impact ejecta/debris could pose issues, and the asteroid's response (e.g., β) from one impact to the next may vary in ways that are difficult to predict.
- KI can only deflect southward.
- While a southward partial deflection via KI is possible in principle, KI is not considered precise/predictable enough to intentionally target a partial southward deflection with confidence on its own.

IBD Strengths:

- IBD requirements and performance are relatively insensitive to asteroid physical properties, other than mass.
- IBD does not pose any risk of asteroid fragmentation.
- IBD is capable of northward or southward deflection.
- IBD is precise enough to target a partial southward deflection with confidence.
- IBD does not require a separate RRS mission.
- IBD is not affected by  nuclear-related legal/policy issues, although legal/policy issues likely exist for any deflection system (even if those issues haven’t been appreciated yet).
- The NEXT-C thruster has been flight-tested (on DART), and previous interplanetary missions such as Dawn and Psyche have demonstrated long-term ion thruster firing in deep space (even though the thrusters were not aimed at an asteroid).

IBD Weaknesses:

- IBD asteroid proximity operations requirements exceed flight heritage (long-term precision pointing, possibly while flying multiple spacecraft in formation near an asteroid, is novel).

- The required SEP power levels and propellant mass for IBD spacecraft are higher than flight heritage (e.g., higher than Psyche or Dawn).
- Asteroid surface material response to ion beam impingement has not yet been demonstrated and characterized in situ.
- There is currently no active production line for the NEXT-C thrusters and Power Processing Units (PPUs). In the case of the purpose-built, 46-kW ARRM-like IBD spacecraft design, it is unclear what would be necessary to reconstitute the NEXT-C thruster and PPU production lines. It is therefore also unclear whether there would be sufficient time before launch to manufacture all the required components and assemble the spacecraft. This is even more of an issue in cases where multiple spacecraft are required.
- The repurposed PPE IBD spacecraft design has thruster and PPU hardware already available, however the PPE design could not simply be used as-is (the BHT thrusters need to be moved to other side of spacecraft, much larger propellant tanks and structure are needed, new onboard control software systems are needed, etc.). This would introduce risks to schedule and mission reliability. Additionally, PPE is currently scheduled to launch in 2028, and so it is unclear whether it would be available to be repurposed for use in a deflection mission like the one in this scenario.

NED Strengths:

- One NED carrier spacecraft carrying 9–12 free-flyer NEDs (100 kt each) is sufficient to deflect the asteroid for any launch opportunity. So, full redundancy could be achieved by launching one additional copy of the spacecraft.
- NED mission launch opportunities span 2029–2035 and can operate on any of the remaining asteroid perihelia before Earth impact (i.e., up to and including the final pre-Earth impact perihelion in 2039).
- The ΔV imparted to the asteroid per detonation can be tuned in situ by simply varying the height of burst (HOB), providing flexibility to respond on-the-fly to knowledge gained in situ about asteroid mass and response to NED detonation.
- The NED carrier mission's asteroid proximity operations requirements are in-family with previous asteroid missions (e.g., OSIRIS-REx). However, 2024 PDC25 is several times smaller (~150 m) than OSIRIS-REx's target asteroid, Bennu (~500 m).
- NEDs are capable of deflecting northward or southward.
- NEDs may be precise enough to target a southward partial deflection with confidence.
- The required SEP spacecraft power levels and propellant mass for the NED carrier spacecraft are in-family with flight heritage, e.g., Psyche.
- The NED option does not require a separate RRS mission.

NED Weaknesses:

- As an impulsive technique, there is some risk of asteroid fragmentation (particularly for this asteroid, which may be a contact binary). Steps taken to avoid fragmentation result in a more complex design involving multiple NED detonations instead of one in some cases.

- The NED carrier spacecraft with multiple free-flying NED sub-spacecraft is a novel design that has not yet been demonstrated and might require additional development time.
- NEDs have been detonated in space (Starfish Prime, 1962), but never flown for an extended period of time in deep space or detonated versus an asteroid. Therefore, there is a lack of flight heritage to build on, and asteroid response to a standoff NED detonation has not been demonstrated and characterized in situ.
- There are significant policy and legal issues associated with launching NED-carrying spacecraft for planetary defense purposes. Demonstrating a strong enough need for NEDs in the situation at hand could overcome legal and policy obstacles to at least some extent, but the rubric for demonstrating such need is not yet clear.

## 9. Conclusions

In this paper, we have described the work performed by our NASA-led team for the 2025 Planetary Defense Conference (PDC) hypothetical asteroid impact threat exercise that is being conducted in coordination with the United Nations-endorsed Space Mission Planning Advisory Group (SMPAG), exercising SMPAG's processes for assessing space mission options and communicating to decision makers.

Our team assessed mission options for asteroid reconnaissance (flyby and rendezvous), deflection, and disruption using several viable techniques: KI, IBD, and NED. Our simulations and analyses considered how much change-in-velocity an asteroid can tolerate before fragmentation onset. We generated an array of feasible asteroid deflection missions, finding that all three techniques studied (KI, IBD, and NED) can provide sufficient asteroid deflection performance, but with very different mission requirements in terms of number of launches, total spacecraft mass, and available launch opportunities.

The ~150-m-size asteroid in this scenario turns out to be challenging to address with KIs because there is a fragmentation risk, and challenging to address with IBD because the asteroid’s mass is large relative to IBD power and time available. This is a result that might not have been expected for a ~150-m-size asteroid with ~17 years of warning time.

Although a single, modestly sized KI could be sufficient to deflect this asteroid if the asteroid could tolerate applied impulses up to ~30% of its escape velocity, the current heuristic specifying the onset of unwanted fragmentation at 10% of the asteroid’s escape velocity results in a cumbersome KI mission campaign design involving multiple spacecraft. The difficulty in predicting asteroid response to multiple KI impacts makes a multiple KI campaign design even more unwieldy and challenging to implement. Meanwhile, even for the median asteroid mass, several IBD spacecraft of ~10,000 kg each would have to be built on relatively short notice. NED deflection, on the other hand, can be accomplished with a single ~6,000 kg NED carrier spacecraft equipped with multiple 100 kt NEDs, across a wide range of launch opportunities. Therefore, NED deflection appears to offer the most robust and feasible technical design, with the lowest mission requirements.

*9.1 Future Work*

A rapid response infrastructure, including both reconnaissance spacecraft and deflection/disruption spacecraft, is needed to facilitate an operational planetary defense capability. Approximately 25% of the 17-year timeline in this scenario was consumed by the construction and deployment of a flyby reconnaissance mission

Asteroid fragmentation risk significantly drives both KI and NED mission design. Hydrocode models that can efficiently run long enough KI/NED simulations are needed to better understand the onset of fragmentation and the requirements for robust disruption, as well as refined heuristics for the same. We also need to better understand what degree of asteroid fragmentation might actually be acceptable during a deflection. Additional KI flight demonstration missions would also be beneficial.

An IBD demonstration mission is also needed and must account for the need to construct potentially rather high mass spacecraft. Also, reliable production lines for critical IBD hardware (e.g., thrusters and PPUs) is needed, along with lower beam divergence thrusters (e.g., NEXT-C or better).

Further assessment of the guidance, navigation, and control needed during the terminal phase of high-speed asteroid intercept missions (for flybys, kinetic impactors, or NED delivery) should be performed. This analysis should include a sensitivity study that quantifies achievable levels of trajectory correction based on asteroid encounter uncertainty and available thruster performance. All of that being said, our team believes that proper guidance and navigation of even relatively massive spacecraft for high-speed asteroid impacts will prove to be doable even if challenging, based on the idea of building on the success of the DART mission.

Finally, a better understanding of how to adjudicate whether a partial deflection into an ocean region would be truly safe and acceptable is needed, and for what range of asteroid impactors (e.g., mass and impact velocity).

**Acknowledgements**

Portions of this exercise were performed under the auspices of the U.S. Department of Energy by Lawrence Livermore National Laboratory under Contract DE-AC52-07NA27344. LLNL-JRNL-2007733. Portions of this exercise were performed under the auspices of the U.S. Department of Energy's NNSA by the Los Alamos National Laboratory, managed by Triad National Security, LLC for the National Nuclear Security Administration of the U.S. Department of Energy under contract 89233218CNA000001. LA-UR-25-23755. D.F. and P.W.C conducted this research at the Jet Propulsion Laboratory, California Institute of Technology, under a contract with the National Aeronautics and Space Administration (80NM0018D0004).

**List of Acronyms**

AEPS - Advanced Electric Propulsion System
ALE - Arbitrary Lagrangian–Eulerian
ARRM - Asteroid Redirect Robotic Mission
ATP - Authority to Proceed
AU - Astronomical Unit
β - Momentum enhancement factor
BHT-6000 -Busek Hall Thruster 6000
ΔV - change-in-velocity
DART - Double Asteroid Redirection Test
DLA (or DEC) - Declination of the Launch Asymptote
EGA - Earth gravity assist
EOL - end-of-life
EOS - Equation of State
FLAG - Free LAGrange
FHE - Falcon Heavy Expendable
HERMeS -Hall Effect Rocket with Magnetic Shielding
HOB - Height of Burst
IAWN - International Asteroid Warning Network
IBD - Ion Beam Deflection
IMC - Implicit Monte Carlo
kW - Kilowatt
KI - Kinetic Impactor
kt - kiloton
LEOS - Livermore Equation of State
LiDAR - Light Detection and Ranging
L to D - launch to deflection time
LV - launch vehicle
M-ANEOS - Melosh ANalytic Equation Of State
Mt - megaton
NASA - National Aeronautics and Space Administration
NED- Nuclear Explosive Device
NEXT-C -NASA Evolutionary Xenon Thruster - Commercial
OSIRIS-APEX- Origins, Spectral Interpretation, Resource Identification and Security – Apophis Explorer
OSIRIS-REx - Origins, Spectral Interpretation, Resource Identification, Security - Regolith Explorer
PDC - Planetary Defense Conference
PPE - Power and Propulsion Element
RAGE - Radiation Adaptive Grid Eulerian
RRS - Rendezvous Reconnaissance Spacecraft
SMPAG - Space Mission Planning Advisory Group
SEP - Solar Electric Propulsion
SES - Sun-Earth-Spacecraft
SESAME - Systematic, Extensive, Standardized, Evaluated Material Equation-of-State
SPH - smoothed particle hydrodynamics
TOF - Time of Flight
VGA - Venus Gravity Assist

XIPS-25 -Xenon Ion Propulsion System (25-cm version)
XR5 - Model designation for Aerojet Rocketdyne 5 kW Hall thruster

**References**


[1] R. Bull, M. Vavrina, J. Lyzhoft, J. Atchison, B. Barbee, 2025. Retasking In-flight Spacecraft for Rapid Response Reconnaissance in Planetary Defense Exercises, 9th IAA Planetary Defense Conference, Stellenbosch, Cape Town, South Africa, May 5-9, 2025

[2] R. Makadia, D. Farnocchia, B. W. Barbee, S. Eggl, 2025. Design Constraints for Asteroid Deflection Campaigns Based on Delta-V Estimation Timelines, 9th IAA Planetary Defense Conference, Stellenbosch, Cape Town, South Africa, May 5-9, 2025

[3] E. J. Christensen, D. Fay, J. B. Fazekas, D. C. Fuls, A. R. Gibbs, A. D. Grauer, B. Gray, H. Groeller, J. K. Hogan, R. A. Kowalski, S. M. Larson, G. J. Leonard, D. Rankin, R. L. Seaman, A. Serrano, F. C. Shelly, J. Sosa, K. W. Wierzchos, 2023. Status of the Catalina Sky Survey, Asteroids, Comets, Meteors Conference, Flagstaff, Arizona, USA, 18-23 June, 2023

[4] A. S. Rivkin, F. Marchis, J. A. Stansberry, D. Takir, C. Thomas, 2016. JWST Asteroids Focus Group, Asteroids and the James Webb Space Telescope, Publications of the Astronomical Society of the Pacific 128, 018003

[5] F. E. DeMeo, R. P. Binzel, S. M. Slivan, S. J. Bus, 2009. An extension of the Bus asteroid taxonomy into the near-infrared, Icarus 202, 160-180

[6] J. L. Dotson, L. Wheeler, D. Mathias, 2024. Consequences of asteroid characterization on the state of knowledge about inferred physical parameters and impact risk, Acta Astronautica 222, 550-555

[7A] L. Wheeler, J. Dotson, M. Aftosmis, A. Coates, G. Chomette, D. Mathias, 2024. Risk assessment for asteroid impact threat scenarios. Acta Astronautica 216, 468–487. https://doi.org/10.1016/j.actaastro.2023.12.049

[7] D. Vokrouhlický, W. F. Bottke, S. R. Chesley, D. J. Scheeres, T. S. Statler, 2015. The Yarkovsky and YORP Effects, Asteroids IV, 509-531, 2015

[8] D. Farnocchia, S. Eggl, P. W. Chodas, J. D. Giorgini, S. R. Chesley, 2019. Planetary encounter analysis on the B-plane: a comprehensive formulation. *Celestial Mechanics and Dynamical Astronomy* 131, 16

[9A] M. J. Berger, D. L. George, R. J. LeVeque, K. T. Mandli, 2011. The GeoClaw software for depth-averaged flows with adaptive refinement. Advances in Water Resources, 34 (9), 1195-1206. https://doi.org/10.1016/j.advwatres.2011.02.016

[9B] M. Boslough, V. Titov, 2024. Air-coupled tsunamis generated from impacts and airbursts: Our understanding before Hunga-Tonga Hunga-Ha'apai, *Acta Astronautica*, Vol. 222, pp. 641–646, https://doi.org/10.1016/j.actaastro.2024.06.041

[9] K. M. Kumamoto, B. W. Barbee, J. Pearl, M. B. Syal, 2024. Probing disruption heuristics for kinetic deflection of asteroids. AGU 2024, NH43D-2445, https://agu.confex.com/agu/agu24/meetingapp.cgi/Paper/1687747

[10] K. M. Kumamoto, B. W. Barbee, J. M. Pearl, M. B. Syal, 2025. Probing heuristics for the kinetic disruption of asteroids, 9th IAA Planetary Defense Conference, Stellenbosch, Cape Town, South Africa, May 5-9, 2025

[11] R. A. Managan, M. T. Burkey, 2023. “Extending NEO Deflection Formulae to High Fluences,” 2023 Planetary Defense Conference, April 3–7, 2023, Vienna, Austria.

[12] M. Burkey, R. Managan, N. Gentile, M. Bruck-Syal, K. Howley, J. Wasem, 2023. X-Ray Energy Deposition Model for Simulating Asteroid Response to a Nuclear Planetary Defense Mitigation Mission. *PSJ*, 4(12):243, December 2023

[13] M. T. Burkey, R. A. Managan, N. Gentile, M. B. Syal, M. Owen, 2023. Initiating Nuclear Mitigation Mission Simulations with a Simplified X-ray Energy Deposition Model, 2023 Planetary Defense Conference, April 3–7, 2023, Vienna, Austria.

[14] N. L. Chabot, J.A. Atchison, R.A. Bull, A.S. Rivkin, R.T. Daly, et.al. “A Mission to Demonstrate Rapid-Response Flyby Reconnaissance for Planetary Defense”, IAC-24-E10.1.1, 75th International Astronautical Congress, Milan, Italy, 2024.

[15] J. M. Owen, J. V. Villumsen, P. R. Shapiro, & H. Martel. 1998, Adaptive Smoothed Particle Hydrodynamics: Methodology II, ApJS, 116, 155, https://doi.org/10.1086/313100

[16] J. M. Owen, 2010. Asph modeling of material damage and failure, in: 5th Spheric International Workshop.

[17] J. M. Pearl, C. D. Raskin, & J. M. Owen. 2022, FSISPH: An SPH Formulation for Impacts between Dissimilar Materials, JCoPh, 469, 111533, https://doi.org/10.1016/j.jcp.2022.111533

[18] D. E. Burton, 1992. Connectivity Structures and Differencing Techniques for Staggered-Grid Free-Lagrange Hydrodynamics. Lawrence Livermore National Laboratory, UCRL-JC-110555.

[19] D. E. Burton, 1994. Consistent Finite Volume Discretization of Hydrodynamic Conservation Laws for Unstructured Grids. Lawrence Livermore National Laboratory, UCRL-JC-118788

[20] J. Hill, 2024. User’s Manual for FLAG version 3.23.11.0. Lagrangian Applications Project, Los Alamos National Laboratory, LA-CP-17-20057
.
[21] W. Benz, & E. Asphaug. 1994, Icar, 107, 98, https://doi.org/10.1006/icar.1994.1009

[22] D. E. Grady, & M. E. Kipp. 1980, International Journal of Rock Mechanics and Mining Sciences & Geomechanics Abstracts, 17, 147, https://doi.org/10.1016/0148-9062(80)91361-3

[23] Collins, G., Melosh, H., Wünnemann, K., 2011. Improvements to the $\epsilon - \alpha$ porous compaction model for simulating impacts into high-porosity solar system bodies.Int. J. Impact Eng. 38 (6), 434–439. http://dx.doi.org/10.1016/j.ijimpeng.2010.10.013

[24] W. Herrmann, 1969. Constitutive equation for the dynamic compaction of ductile porous materials. J. Appl. Phys. 40, 2490–2499. https://doi.org/10.1063/1.1658021

[25] M. Jutzi, W. Benz, P. Michel, 2008. Numerical simulations of impacts involving porous bodies. I. Implementing sub-resolution porosity in a 3D SPH hydrocode. Icarus 198, 242–255. https://doi.org/10.1016/j.icarus.2008.06.013

[26] K. Wünnemann, G. Collins, H. Melosh, 2006. A strain-based porosity model for use in hydrocode simulations of impacts and implications for transient crater growth in porous targets. Icarus 180 (2), 514–527. http://dx.doi.org/10.1016/j.icarus.2005.10.013

[27] A. M. Stickle, *et al.* 2025, *Planet. Sci. J.* **6** 38**,** https://doi.org/10.3847/PSJ/ad944d

[28] W. K. Caldwell, A. Hunter, C. S. Plesko, S. Wirkus, 2018. Verification and Validation of the FLAG Hydrocode for Impact Cratering Simulations. Journal of Verification, Validation and Uncertainty Quantification, 3(3):031004.

[29] A. M. Stickle *et al.*, 2022. PSJ **3** 11.

[30] K. M. Kumamoto, J. M. Owen, M. B. Syal, et al. 2022, Predicting Asteroid Material Properties from a DART-like Kinetic Impact, PSJ, 3, 237, https://doi.org/10.3847/PSJ/ac93f2

[31] W. K. Caldwell, 2019. Differential Equation Models for Understanding Phenomena beyond Experimental Capabilities. Arizona State University.

[32] W. K. Caldwell, A. Hunter, C. S. Plesko, S. Wirkus, 2020. Understanding Asteroid 16 Psyche's Composition through 3D Impact Crater Modeling. Icarus 351:113962.

[33] M. Holmes, W. K. Caldwell, J. Budzien, C. E. Johnson, 2024. Using Hydrodynamic Similarity as a Verification Method for Impact Cratering Simulations in the FLAG Hydrocode. PSJ 5:150.

[34] W. K. Caldwell, A. Hunter, C. S. Plesko, 2024. Exploring Density and Strength Variations in Asteroid 16 Psyche's Composition with 3D Hydrocode Modeling of Its Deepest Impact Structure. Icarus 408:115780.

[35] S. F. Henderson, A. Padilla, W. K. Caldwell, E. Rougier, Z. Lei, M. R. Sweeney, P. H. Stauffer, 2025. Modeling the Formation of Sedan Crater using the FLAG and HOSS Codes. Scientific Reports.

[36] F. N. Fritsch. 2016, LIP: The Livermore Interpolation Package, Version 1.6 LLNL-TR-406719-REV-5, Lawrence Livermore National Laboratory, https://www.osti.gov/biblio/1234602

[37] S. L. Thompson, H. S. Lauson, H. J. Melosh, G. S. Collins, & S. T. Stewart, 2019. M-ANEOS: A Semi-Analytical equation of State Code, v1, Zenodo, https://doi.org/10.5281/zenodo.3525030

[38] C. Raskin, J. Owen, 2016. Rapid optimal SPH particle distributions in spherical geometries for creating astrophysical initial conditions. Astrophys. J. 820 (2), 1–7. http://dx.doi.org/10.3847/0004-637X/820/2/102

[39] S. P. Lyon and J. D. Johnson, 1992. SESAME: The Los Alamos National Laboratory Equation of State Database. Los Alamos National Laboratory, LA-UR-92-3407.

[40] D. Zaytsev, E. N. Borodin, A. E. Dudorov, P. Panfilov, 2021. The mechanical properties of Chelyabinsk LL5 Chondrite under compression and tension. Earth Moon Planets 125 (1), http://dx.doi.org/10.1007/s11038-021-09539-x

[41] Rabbi et.al., 2021. Understanding asteroidal failure through quasi-static compression testing and 3-D digital image correlation of the Aba Panu (L3) chondrite, Meteoritics & Planetary Science, 56, https://doi.org/10.1111/maps.13761

[42] D. R. Stephens & E. M. Lilley. 1970, Compressibilities of lunar crystalline rock, microbreccia, and fines to 40 kilobars. Science 167, 731–732. https://doi.org/10.1126/science.167.3918.731

[43] S. D. Raducan, M. Jutzi, A. F. Cheng, et al. 2024, Physical Properties of Asteroid Dimorphos as Derived from the DART Impact, NatAs, 8, 445. https://doi.org/10.1038/s41550-024-02200-3

[44] R. Darlington, T. McAbee, G. Rodrigue, 2001. A study of ALE simulations of Rayleigh-Taylor instability. *Computer Physics Communications.* 135(1): 58-73

[45] J. Bender, O. Schilling, K. Raman, R. Managan, B. Olson, S. Copeland, C. Ellison, D. Erskine, C. Huntington, B. Morgan, et al. 2021. Simulation and flow physics of a shocked and reshocked high-energy-density mixing layer. *Journal of Fluid Mechanics,* 915:A84

[46] Barnes, John F., and Stanford P. Lyon. *SESAME equation of state No. 7530, basalt*. No. LA-11253-MS. Los Alamos National Lab.(LANL), Los Alamos, NM (United States), 1988.

[47] Masser, Thomas, et al. "Verification and Validation of cassio, an HEDP Code from the Crestone Project." *APS Division of Plasma Physics Meeting Abstracts*. Vol. 50. 2008.

[48] Gittings, Michael, et al. "The RAGE radiation-hydrodynamic code." *Computational Science & Discovery* 1.1 (2008): 015005.
[49] Falk, Katerina, et al. "Temperature measurements of shocked silica aerogel foam." *Physical Review E* 90.3 (2014): 033107.

[50] Park, H., et al. "Moment-based acceleration of Monte Carlo solution for multifrequency thermal radiative transfer problems." *Journal of computational and theoretical transport* 43.1-7 (2014): 314-335.